The Astrophysical Journal, 823:128 (18pp), 2016 June 1 doi:10.3847/0004-637X/823/2/128

THE QUEST FOR DUSTY STAR-FORMING GALAXIES AT HIGH REDSHIFT $z \gtrsim 4$

C. Mancuso[1,2,3], A. Lapi[1,2,3], J. Shi[1,4], J. Gonzalez-Nuevo[5], R. Aversa[1,3], and L. Danese[1,2,3]
[1] SISSA, Via Bonomea 265, I-34136 Trieste, Italy
[2] INAF-Osservatorio Astronomico di Trieste, via Tiepolo 11, I-34131 Trieste, Italy
[3] INFN-Sezione di Trieste, via Valerio 2, I-34127 Trieste, Italy
[4] Key Laboratory for Research in Galaxies and Cosmology, Department of Astronomy, University of Science and Technology of China, Hefei, 230026 Anhui, China
[5] Departamento de Física, Universidad de Oviedo, C. Calvo Sotelo s/n, E-33007 Oviedo, Spain
Received 2015 November 5; accepted 2016 April 8; published 2016 May 31

ABSTRACT

We exploit the continuity equation approach and "main-sequence" star formation timescales to show that the observed high abundance of galaxies with stellar masses $\gtrsim$ a few $10^{10}\,M_\odot$ at redshift $z \gtrsim 4$ implies the existence of a galaxy population featuring large star formation rates (SFRs) $\psi \gtrsim 10^2\,M_\odot\,\mathrm{yr}^{-1}$ in heavily dust-obscured conditions. These galaxies constitute the high-redshift counterparts of the dusty star-forming population already surveyed for $z \lesssim 3$ in the far-IR band by the *Herschel Space Observatory*. We work out specific predictions for the evolution of the corresponding stellar mass and SFR functions out to $z \sim 10$, determining that the number density at $z \lesssim 8$ for SFRs $\psi \gtrsim 30\,M_\odot\,\mathrm{yr}^{-1}$ cannot be estimated relying on the UV luminosity function alone, even when standard corrections for dust extinction based on the UV slope are applied. We compute the number counts and redshift distributions (including galaxy-scale gravitational lensing) of this galaxy population, and show that current data from the *AzTEC-LABOCA*, *SCUBA-2*, and *ALMA-SPT* surveys are already addressing it. We demonstrate how an observational strategy based on color preselection in the far-IR or (sub-)millimeter band with *Herschel* and *SCUBA-2*, supplemented by photometric data from on-source observations with *ALMA*, can allow us to reconstruct the bright end of the SFR functions out to $z \lesssim 8$. In parallel, such a challenging task can be managed by exploiting current UV surveys in combination with (sub-)millimeter observations by *ALMA* and *NIKA2* and/or radio observations by *SKA* and its precursors.

Key words: dust, extinction – galaxies: abundances – galaxies: evolution – infrared: galaxies

1. INTRODUCTION

Star formation in galaxies can be inferred by lines like Lyα and Hα, and by continuum emission in the ultraviolet (UV), infrared (IR), radio, and X-ray bands (see Kennicutt & Evans 2012 for a review). In the local universe, a significant fraction of the star formation in galaxies occurs in dust-enshrouded environments (e.g., Carilli et al. 2013; Madau & Dickinson 2014), with a clear tendency for dust extinction to become more severe as the star formation rate (SFR) increases. Dust causes the UV emission from young massive stars, which traces the SFR, to be absorbed and reradiated in the far-IR band; thus, a combined measurement of the UV and far-IR luminosities would constitute a sound probe of the SFR.

Even at high-redshift, dusty star-forming galaxies are quite common, as shown by the large surveys obtained by ground- and space-based instruments in recent years (for a review, see Casey et al. 2014). The tendency for dust obscuration to increase with SFR is also confirmed by the increase of the UV-continuum slope $\beta_{\rm UV}$ with rising luminosity in UV-selected galaxies up to $z \sim 8$ (see Bouwens et al. 2014 and references in their Figure 1; also Reddy et al. 2012; Coppin et al. 2015).

The correlation of the UV slope $\beta_{\rm UV}$ with the IR to UV luminosity ratio (dubbed the IRX ratio) in star-forming galaxies has commonly been exploited in order to estimate their dust absorption (e.g., Meurer et al. 1999). As a matter of fact, far-IR observations of UV-selected galaxies confirmed that estimates of dust attenuation based on the $\beta_{\rm UV}$–IRX correlation are reliable for objects with SFR $\psi \lesssim 30\,M_\odot\,\mathrm{yr}^{-1}$ (e.g., Lee et al. 2012; Reddy et al. 2012, 2015; Coppin et al. 2015). On the other hand, the scatter of the $\beta_{\rm UV}$–IRX relation largely widens with increasing $\beta_{\rm UV}$ and IRX (i.e., with increasing SFR on average), making the dust correction quite uncertain for SFR $\psi \gtrsim 30\,M_\odot\,\mathrm{yr}^{-1}$ (e.g., Chapman et al. 2000; Goldader et al. 2002; for a recent review, see Conroy 2013).

The relevance of dust absorption is evident from the shape and redshift evolution of the luminosity function at the bright end (e.g., Mao et al. 2007; Bouwens et al. 2009; Cai et al. 2014; Bowler et al. 2015). More precisely, the uncertainty in dust absorption strongly affects the estimate of the SFR function at the bright end, as inferred from UV surveys. At redshifts up to $z \sim 3$, this effect has been statistically quantified by Aversa et al. (2015) by comparing the SFR function as inferred from the UV luminosity function (corrected for the dust absorption based on the UV slope) with that inferred from the far-IR surveys conducted with the SPIRE instrument on board *Herschel* (see Lapi et al. 2011; Gruppioni et al. 2013, 2015; Magnelli et al. 2013). These authors have shown that UV surveys start to undersample galaxies with SFR $\psi \gtrsim 30\,M_\odot\,\mathrm{yr}^{-1}$, even when corrected for dust attenuation on the basis of the UV slope–IRX correlation. They have also highlighted that the galaxy stellar mass function at $z \lesssim 3$ can be recovered from the intrinsic SFR function. At higher redshifts, $z \gtrsim 3$, direct comparison is hampered by the fact that while the UV luminosity function is soundly determined up to redshift $z \sim 8$ (e.g., Bouwens et al. 2015; Bowler et al. 2015; Finkelstein et al. 2015a), the far-IR luminosity function is not yet available due to the sensitivity limits of current instruments.

To circumvent this problem, Aversa et al. (2015) have argued that the continuity equation applied to the SFR and stellar mass can provide an important clue as to the distribution of the intrinsic SFR even at $z \gtrsim 4$. In this vein, it is worth noting that the spectral energy distribution (SED) for large samples of high-redshift galaxies has recently been determined

for the UV to near-/mid-IR, allowing for a sound estimate of the photometric redshift, stellar mass, dust extinction, SFR, and age of stellar populations (e.g., Duncan et al. 2014; Speagle et al. 2014; Caputi et al. 2015; Grazian et al. 2015; Salmon et al. 2015; Stefanon et al. 2015), with some caveats related to the degeneracy among these parameters (e.g., Conroy 2013).

An estimate of the galaxy stellar mass function at substantial redshift has been obtained by combining the observed mass-to-UV light ratio and the UV luminosity function (e.g., Stark et al. 2009; González et al. 2011; Lee et al. 2012; Song et al. 2015). However, both of these key ingredients are expected to be affected by dust extinction at high UV luminosity. Moreover, the correlation $M_\star$–$M_{\rm UV}$ is largely scattered. Note that such a relation is also relevant for the definition of the so-called "main sequence," once the UV luminosity is translated into the SFR, provided that the dust effects are properly taken into account.

Bypassing the UV selection, deep optical/near-IR/mid-IR imaging provided by the *Hubble Space Telescope* (*HST*), *Spitzer*, and the Very Large Telescope for the CANDELS-UDS, GOODS-South, and HUDF fields has recently been exploited in order to determine the galaxy stellar mass function at redshift $z \gtrsim 3$, with the stellar mass derived from the SED fitting technique including nebular emission (Duncan et al. 2014; Grazian et al. 2015; also Caputi et al. 2015). The stellar mass function has been computed by weighting the galaxies with the $1/V_{\rm max}$ Schmidt's estimator (Schmidt 1968). The result agrees with that derived only for UV-selected galaxies when a large intrinsic scatter $\gtrsim$0.5 dex in the $M_\star$–$M_{\rm UV}$ relation is assumed (see Figure 9 in Duncan et al. 2014). Such a wide scatter suggests that a fraction of the low-luminosity UV-selected galaxies are already massive, and that either they are already quiescent or they form most of their stars within a dusty interstellar medium (ISM; see also Grazian et al. 2015). As a matter of fact, Song et al. (2015) note the increase of massive but faint UV galaxies at lower redshift, suggesting that the role of dust becomes increasingly relevant with cosmic time. Also, Bowler et al. (2015) point out that the bright end of the UV luminosity function appears to steepen from $z \sim 7$ to 5, which may suggest the onset of dust obscuration. Additional evidence for the presence of dust at quite high redshift is confirmed by observations of quasars (e.g., Bolton et al. 2011), direct detection from *ALMA* (e.g., Weiss et al. 2013; Swinbank et al. 2014; da Cunha et al. 2015), and indirectly from the nature of high-z gamma-ray bursts (e.g., Schady et al. 2014).

In this paper, we aim to determine the intrinsic SFR and stellar mass functions, unbiased with respect to dust obscuration; these are indeed crucial ingredients for our physical understanding of galaxy formation and evolution. For example, these functions can be used to obtain the *intrinsic* relationships of the SFR/stellar mass versus the dark matter (DM) halo mass via the abundance matching technique (e.g., Vale & Ostriker 2004; Shankar et al. 2006; Behroozi et al. 2013; Moster et al. 2013). We will see that exploiting such intrinsic relationships, as opposed to those derived after dust corrections based on the UV slope, naturally leads to solving several critical issues in galaxy formation and evolution, as pointed out by Steinhardt et al. (2015) and Finkelstein et al. (2015b): the former authors claim that massive high-redshift galaxies formed impossibly early according to standard models of galaxy assembly; the latter authors point out an unexpected increase of the stellar to baryon fraction in bright galaxies at high redshift.

The plan of this paper is as follows. In Section 2, we develop a new method to obtain an analytic rendition of the intrinsic SFR function at any redshift in the range $z \sim 0$–10 based on the most recent UV and far-IR data. In Section 2.1, we validate our intrinsic SFR function by comparison with the observed (sub-) millimeter counts, redshift distributions, and cosmic infrared background. In Section 2.2, we exploit the continuity equation approach to further validate our intrinsic SFR function by comparison with the observed stellar mass function at high redshift $z \gtrsim 4$. In Section 3, we use the abundance matching technique to derive the relationships between SFR and stellar mass versus halo mass, and we discuss their consequences for galaxy formation scenarios. In Section 4, we design specific observational strategies to hunt for high-z dusty galaxies which we predict populate the bright end of the intrinsic SFR function for $z \gtrsim 4$ by exploiting far-IR/(sub-)millimeter (Section 4.1) and/or UV surveys (Section 4.2). Finally, in Section 5, we summarize our results.

Throughout this work we adopt the standard flat concordance cosmology (Planck Collaboration XIII 2015) with round parameter values: matter density $\Omega_M = 0.32$, baryon density $\Omega_b = 0.05$, Hubble constant $H_0 = 100\,h\,{\rm km\,s^1\,Mpc^1}$ with $h = 0.67$, and mass variance $\sigma_8 = 0.83$ on a scale of $8\,h^{-1}$ Mpc. The stellar masses and luminosities (or SFRs) of galaxies are evaluated assuming the Chabrier (2003) initial mass function (IMF).

2. RECONSTRUCTING THE INTRINSIC SFR FUNCTION

From an observational point of view, the intrinsic SFR function $N(\log\psi, z)$, namely, the number of galaxies per logarithmic bin of SFR $[\log\psi, \log\psi + d\log\psi]$ at a given redshift z, is mainly determined from pure UV or pure far-IR selected samples; in both cases, *corrections* come into play and must be taken into proper account to infer the intrinsic SFR function. When based solely on IR measurements, the main issue concerns the contribution to the global IR luminosity coming from diffuse dust (cirrus), which reprocesses the light from less massive, older stars; in fact, the SFR is better traced by the dust emission from molecular clouds, which instead reprocesses the UV light from young, massive stars. Not correcting the global luminosity for diffuse (cirrus) emission would cause the SFR to be appreciably overestimated; however, this is not an easy task since diffuse emission depends on several aspects such as stellar mass, galaxy age, chemical composition, the amount of dust, and related spatial distribution (see Silva et al. 1998). On the other hand, several studies in the local universe (e.g., Hao et al. 2011; Clemens et al. 2013; Rowlands et al. 2014) have demonstrated that cold diffuse emission is relevant mainly for SFRs $\psi \lesssim 30\,M_\odot\,{\rm yr}^{-1}$, but becomes less and less important at higher SFRs $\psi \gtrsim 10^2\,M_\odot\,{\rm yr}^{-1}$. The same conclusion holds for high-redshift $z \sim 1.5$–3 star-forming galaxies with SFR $\psi \gtrsim 30\,M_\odot\,{\rm yr}^{-1}$, as can be seen from the analysis of the ALESS survey by Swinbank et al. (2014) and da Cunha et al. (2015, see their Figure 10), who find dust temperatures in excess of 30 K.

When based solely on UV measurements, the main concern is to correct for dust extinction. One of the most common methods is to exploit the correlation between the UV slope $\beta_{\rm UV}$ and the IRX ratio as gauged in the local universe (e.g., Meurer et al. 1999; Reddy et al. 2012; Bouwens et al. 2015). However,

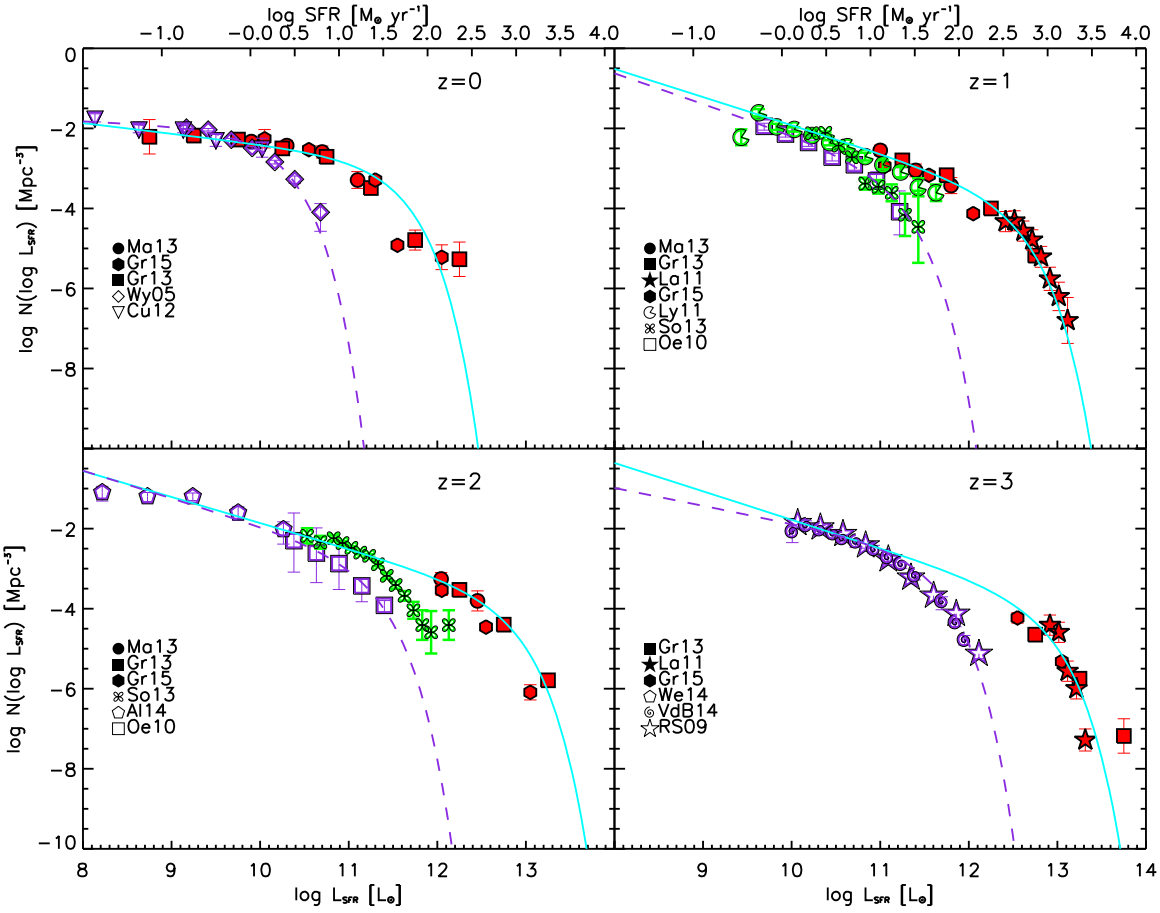

Figure 1. SFR function at redshifts $z \approx 0$–3. Solid cyan lines illustrate our fits to the intrinsic (IR+UV) SFR functions, while violet dashed lines refer to the UV-inferred SFR functions. UV data (dust-corrected; violet symbols) are from Wyder et al. (2005; open diamonds), Cucciati et al. (2012; open inverse triangles), Oesch et al. (2010; open squares), Alavi et al. (2014; open pentagons), Reddy & Steidel (2009; open stars), and van der Burg et al. (2010; spirals); Hα data (green symbols) are from Ly et al. (2011; pacmans) and Sobral et al. (2013; clovers); and IR data (red symbols) come from Magnelli et al. (2013; filled circles), Gruppioni et al. (2013; filled squares), Gruppioni et al. (2015; filled hexagons), and Lapi et al. (2011; filled stars).

for SFRs $\psi \gtrsim 30\,M_\odot\,\mathrm{yr}^{-1}$, when the attenuation becomes appreciable, the $\beta_{\rm UV}$–IRX correlation is found to be extremely dispersed, resulting in a very uncertain estimate of the attenuation even in local samples (e.g., Howell et al. 2010; Reddy et al. 2015). On the other hand, the correlation is found to be less scattered for SFRs $\psi \lesssim 30\,M_\odot\,\mathrm{yr}^{-1}$, and the dust correction to the UV luminosity becomes more secure and relatively small on average. This is also suggested by the UV attenuation inferred by combining Hα measurements with the Calzetti extinction curve (e.g., Mancuso et al. 2015; Reddy et al. 2015).

Given these considerations, we build the intrinsic SFR function $N(\log\psi, z)$ as follows. We start from the most recent determinations of the luminosity functions at different redshifts from far-IR and UV data (the latter being dust-corrected according to the $\beta_{\rm UV}$–IRX relation; see Meurer et al. 1999; Bouwens et al. 2009, 2015); the outcome is illustrated in Figure 1. The SFR ψ and the associated luminosity L_ψ reported for the upper and lower axis are related assuming the calibration

$$\log\frac{\psi}{M_\odot\,\mathrm{yr}^{-1}} \approx -9.8 + \log\frac{L_\psi}{L_\odot}, \qquad (1)$$

which approximately holds for a Chabrier IMF both for far-IR and (intrinsic) UV luminosities (see Kennicutt & Evans 2012).

At redshift $z \lesssim 3$, we lack a robust determination of the SFR function at intermediate values of the SFR. On the one hand, UV data almost disappear for SFRs $\psi \gtrsim 30\,M_\odot\,\mathrm{yr}^{-1}$ because of dust extinction (with dust corrections becoming progressively uncertain, as discussed above). On the other hand, far-IR data progressively disappear for SFRs $\lesssim 10^2\,M_\odot\,\mathrm{yr}^{-1}$ because of current observational limits. At higher redshift, $z \gtrsim 4$, once again UV surveys can provide reliable estimate of the SFR function for SFRs $\psi \lesssim 30\,M_\odot\,\mathrm{yr}^{-1}$, but we lack far-IR data deep enough to statistically probe the high end of the SFR.

To obtain an analytic rendition of the intrinsic SFR function in the full range of SFRs $\psi \sim 10^{-1}$—several $10^3\,M_\odot\,\mathrm{yr}^{-1}$ and redshift $z \sim 0$–10—we perform a least-χ^2-fit to the data with a standard Schechter functional shape:

$$N(\log\psi) = \mathcal{N}(z)\left[\frac{\psi}{\psi_c(z)}\right]^{1-\alpha(z)} e^{-\psi/\psi_c(z)}\,. \qquad (2)$$

The fit is educated, which means that for redshift $z \lesssim 3$ where both UV and far-IR data are present, we consider the UV data (dust-corrected according the $\beta_{\rm UV}$–IRX ratio) to be reliable for SFRs $\psi \lesssim 30\,M_\odot\,\mathrm{yr}^{-1}$, and the far-IR data for SFRs $\psi \gtrsim 10^2\,M_\odot\,\mathrm{yr}^{-1}$. As for higher redshift, we make the assumption that at $z \gtrsim 8$, the (dust-corrected) UV data are reliable estimators of the intrinsic SFR function. This assumption relies

Table 1
SFR Function Parameters

Parameter	Intrinsic				UV (Dust-corrected)			
	p_0	p_1	p_2	p_3	p_0	p_1	p_2	p_3
$\log \mathcal{N}(z)$	-2.48 ± 0.06	-6.55 ± 1.17	12.98 ± 3.49	-8.19 ± 2.48	-1.96 ± 0.07	-1.60 ± 1.44	4.22 ± 3.66	-5.23 ± 2.48
$\log \psi_c(z)$	1.25 ± 0.05	5.14 ± 0.60	-3.22 ± 1.64	-1.81 ± 1.16	0.01 ± 0.05	2.85 ± 0.94	0.43 ± 2.40	-1.70 ± 1.61
$\alpha(z)$	1.27 ± 0.01	2.89 ± 0.23	-6.34 ± 0.66	4.33 ± 0.46	1.11 ± 0.02	2.85 ± 0.48	-6.18 ± 1.26	4.44 ± 0.83

Note. Quoted uncertainties are at the 1σ level. Fits hold in the range SFR $\psi \sim 10^{-2}$–$10^{4}\, M_{\odot}\, \mathrm{yr}^{-1}$ and redshifts $z \sim 0$–8.

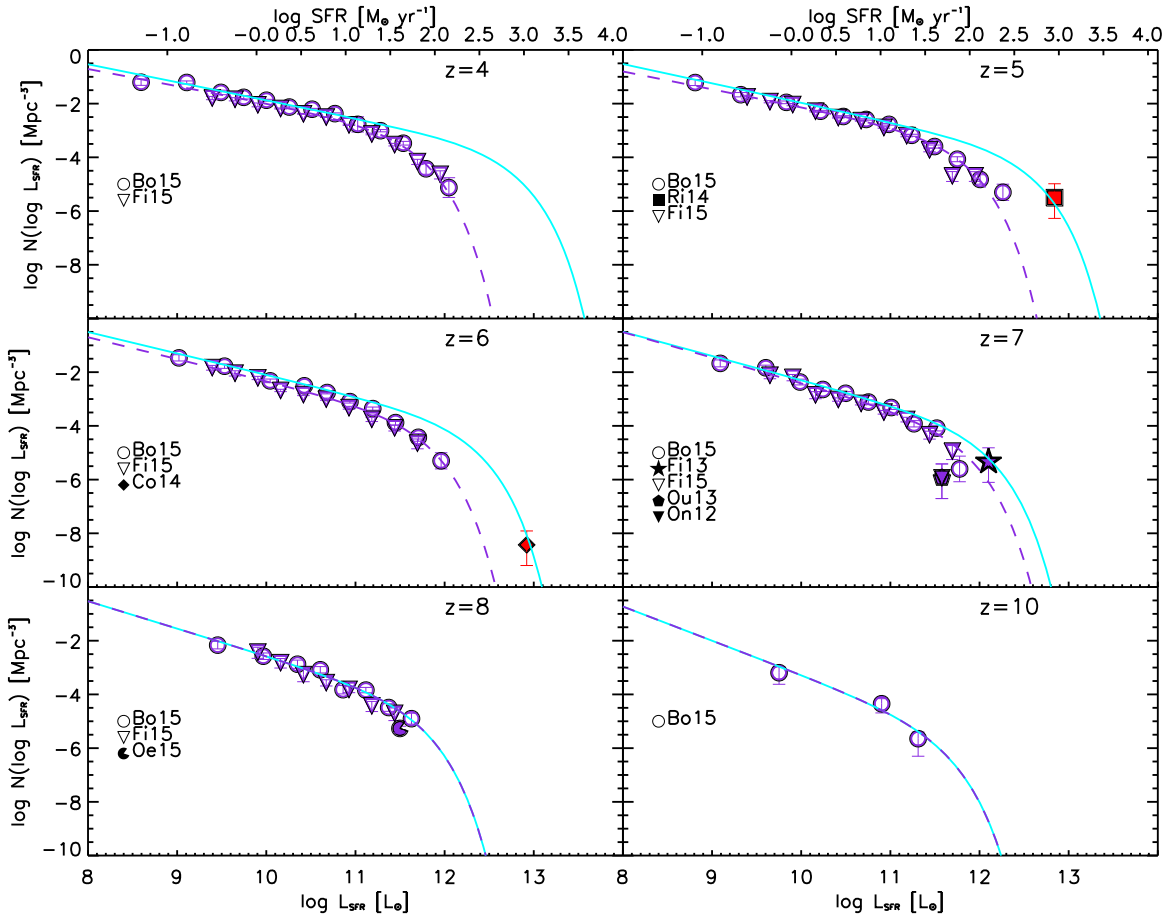

Figure 2. Same as previous figure, but for redshifts $z \approx 4$–10. Solid cyan lines illustrate our determination of the intrinsic (IR+UV) SFR functions, while violet dashed lines illustrate our fits to the UV-inferred SFR function. UV data (dust-corrected; violet symbols) are from Bouwens et al. (2015; open circles) and Finkelstein et al. (2015a; open inverse triangles). Filled symbols represent the number density associated with the detection of individual galaxies with spectroscopic redshift determination (see text for details): violet ones refer to galaxies selected in UV/Lyα from Finkelstein et al. (2013; star), Ouchi et al. (2013; pentagon), Ono et al. (2012; inverse triangle), and Oesch et al. (2015; pacman); red ones refer to galaxies selected in IR/sub-millimeter from Riechers et al. (2014; square) and Cooray et al. (2014; diamond).

on the fact that with an age of the universe shorter than 6×10^8 years, the amount of dust in a star-forming galaxy is expected to be rather small (see Section 4.2).

Equipped with such values of the Schechter parameters at redshift $z \lesssim 3$ and $z \gtrsim 8$, we fit their evolution with a polynomial in log-redshift; in other words, for any parameter $p(z)$ of the Schechter function, say $\mathcal{N}(z)$, $\psi_c(z)$, or $\alpha(z)$, we fit for the functional shape

$$p(z) = p_0 + p_1\, \xi + p_2\, \xi^2 + p_3\, \xi^3, \qquad (3)$$

where $\xi \equiv \log(1+z)$. The outcomes of the fits are reported in Table 1.

This procedure, based on the assumption of the analytical continuity of the intrinsic SFR function, yields a result that works pleasingly well for $z \lesssim 3$ and $z \gtrsim 8$, see Figures 1 and 2; moreover, we end up with an estimate for the behavior of the SFR function at $z \sim 4$–8 where sampling by far-IR surveys is absent. In such a redshift range, this estimate implies a significant number density of dusty star-forming galaxies with SFR $\psi \gtrsim 10^2\, M_{\odot}\, \mathrm{yr}^{-1}$, which is currently missed by UV data (even corrected for dust extinction). To highlight this point more clearly, in Figures 1 and 2 we also report the SFR function that would have been inferred based solely on dust-corrected UV data over the full redshift range $z \approx 0$–10. Clearly, at any redshift $z \lesssim 7$, the UV data, even corrected for

dust extinction based on the UV slope, strongly underestimate the intrinsic SFR function for SFRs $\psi \gtrsim 30\,M_\odot\,\mathrm{yr}^{-1}$.

Circumstantial evidence for such a population of dusty star-forming galaxies at $z \gtrsim 4$ has accumulated in recent years. Riechers et al. (2014) detected a dust-obscured galaxy at $z \approx 5.3$ with SFR $\psi \approx 1100\,M_\odot\,\mathrm{yr}^{-1}$ and stellar mass $M_\star \approx 10^{10}\,M_\odot$. Cooray et al. (2014) detected a second one at $z \approx 6.34$ with SFR $\psi \approx 1320\,M_\odot\,\mathrm{yr}^{-1}$ and stellar mass $M_\star \approx 5 \times 10^{10}\,M_\odot$. It is remarkable that the inferred number densities for these objects, though within the considerable uncertainties, agree with the prediction of our intrinsic SFR function, while being substantially higher than the expectations from the purely UV-inferred one (see Figure 2).

At lower levels of SFRs, moderately dusty galaxies start to be selected even in the UV, especially at high redshift $z \gtrsim 7$. For example, Finkelstein et al. (2013) detected one at $z \approx 7.51$ with SFR $\psi \approx 200\,M_\odot\,\mathrm{yr}^{-1}$ and stellar mass $M_\star \approx 6 \times 10^8\,M_\odot$. Oesch et al. (2015) revealed one at $z \approx 7.73$ with SFR $\psi \approx 30$–$50\,M_\odot\,\mathrm{yr}^{-1}$ and stellar mass $M_\star \approx 5 \times 10^9\,M_\odot$. Ouchi et al. (2013) detected another one at $z \approx 6.6$ with SFR $\psi \approx 60\,M_\odot\,\mathrm{yr}^{-1}$ and stellar mass $M_\star \approx 10^{10}\,M_\odot$. Ono et al. (2012) detected one at $z \approx 7.2$ with SFR $\psi \approx 60\,M_\odot\,\mathrm{yr}^{-1}$ and stellar mass $M_\star \approx 3 \times 10^8\,M_\odot$. An intense search is currently ongoing, with an appreciable number of candidates being found (see Roberts-Borsani et al. 2015; Zitrin et al. 2015). The number densities of these galaxies are consistent with the UV-corrected SFR function, which at these high redshift approaches the intrinsic one.

We stress that while the focus of the present paper is mainly on the bright portion of the intrinsic SFR function at high redshift, the faint end as sampled by UV data is essential for understanding important issues both in astrophysics and cosmology, such as the history of cosmic reionization (e.g., Cai et al. 2014; Robertson et al. 2015), and even in fundamental physics, such as the nature of DM (e.g., Lapi & Danese 2015).

2.1. Validating the Intrinsic SFR Function via the (Sub-) Millimeter Counts

We aim to validate our intrinsic SFR function via a comparison with the observed (sub-)millimeter counts, redshift distributions, and cosmic infrared background. We compute the counts according to the expression (see Lapi et al. 2011)

$$\frac{dN}{d\log S_\nu\,d\Omega}(S_\nu) = \int dz\,\frac{dV}{dz\,d\Omega}\,N(\log\psi)\,\frac{d\log\psi}{d\log S_\nu}, \tag{4}$$

in terms of the flux

$$S_\nu = \frac{L_{\nu(1+z)}}{L_\psi}\,\frac{(1+z)}{4\pi\,D_L^2(z)}; \tag{5}$$

in the above, $N(\log\psi)$ is the SFR function, $dV/dz\,d\Omega$ is the cosmological volume per redshift bin and unit solid angle, L_ψ is the bolometric luminosity associated with the SFR ψ according to Equation (1), and $L_{\nu(1+z)}/L_\psi$ is the K-correction. The latter has been computed based on the SED typical of a high-redshift, dust-obscured, star-forming galaxy; specifically, we consider as a reference the SED of the "Cosmic Eyelash" (SMM J2135 +0102; see Ivison et al. 2010; Swinbank et al. 2010), but we will show the impact of assuming a different SED. Actually, for the sources located at $z \lesssim 0.3$ and contributing only to the very bright counts probed by Planck Collaboration VII (2013), we have adopted the warmest SED from the template library of Smith et al. (2012).

We have also evaluated the contribution to the counts from strong galaxy-scale gravitational lensing, according to the SISSA model (see Lapi et al. 2012); the lensed counts are computed as

$$\frac{dN_{\rm lensed}}{d\log S_\nu\,d\Omega}(S_\nu) = \int dz\,\frac{1}{\langle\mu\rangle}\int_2^{\mu_{\rm max}} d\mu \times \frac{dp}{d\mu}(\mu, z)\,\frac{dN_{\rm unlensed}}{d\log S_\nu\,d\Omega\,dz}(S_\nu/\mu, z). \tag{6}$$

Here, $dp/d\mu$ is the amplification distribution and $\langle\mu\rangle$ is its average ($\approx$1 for a wide-area survey); a maximum amplification of $\mu_{\rm max} \approx 25$ has been adopted (see Cai et al. 2013; Bonato et al. 2014).

The Euclidean-normalized, differential counts at various wavelengths $\lambda \approx 500$, 850, 1100, and 1400 μm are plotted in Figure 3. We find an excellent agreement between the counts derived from our intrinsic SFR function and various observational data (see the details in the caption). In contrast, we also show that the counts expected from the UV-inferred SFR function considerably underpredict the data at the bright end. Note that to make the contribution to the counts from the UV-inferred SFR function as large as possible, we have assumed that all of the UV emission is reprocessed by dust and reradiated in the far-IR according to the coldest SED from the template library by Smith et al. (2012).

We note that the counts at $\lambda \gtrsim 850\,\mu$m for fluxes $\gtrsim$ several mJy are primarily contributed by galaxies located at $z \gtrsim 3$. This is shown in detail by the redshift distributions presented in Figure 4, which peak at $z \approx 3$–4 with a substantial tail at higher z. Specifically, we find a pleasing agreement of our results based on the intrinsic SFR function with the 1400 μm *ALMA-SPT* data at a flux limit of $\gtrsim$20 mJy, constructed from a sample of 26 galaxies with spectroscopic redshifts (Weiss et al. 2013; see also Strandet et al. 2016). The redshift distribution is essentially contributed by gravitationally lensed sources, and it constitutes an extremely important test of the intrinsic SFR function up to $z \approx 6$. Note that the lensed counts would be strongly underestimated when based on the (dust-corrected) UV-inferred SFR function (see Figure 3, bottom right panel). We also find good agreement with the 850 μm data from *SCUBA-2* by Koprowski et al. (2016) at a limiting flux of $\gtrsim$2 mJy, and from *AzTEC-LABOCA* data by Koprowski et al. (2014; see also Smolcic et al. 2012) at a flux limit of $\gtrsim$8 mJy, which constitute a sample of about 100 sources with mostly photometric redshifts.

In Figure 5, we show that the cosmic infrared background at 500, 850, and 1400 μm as derived from our intrinsic SFR function is consistent with the measurements by Fixsen et al. (1998; see also Lagache et al. 1999; Planck Collaboration XVIII 2011; Planck Collaboration XXX 2014). As extensively discussed by Lapi et al. (2011; see their Figure 19), the evolution with redshift of the background highlights that, for $\lambda \gtrsim 500\,\mu$m, it is mostly contributed by high-redshift galaxies down to $z \approx 2$–3. This trend strengthens as λ increases; in particular, at 1400 μm, about 50% of the background is contributed by dusty galaxies at $z \gtrsim 3$; this fraction would drop

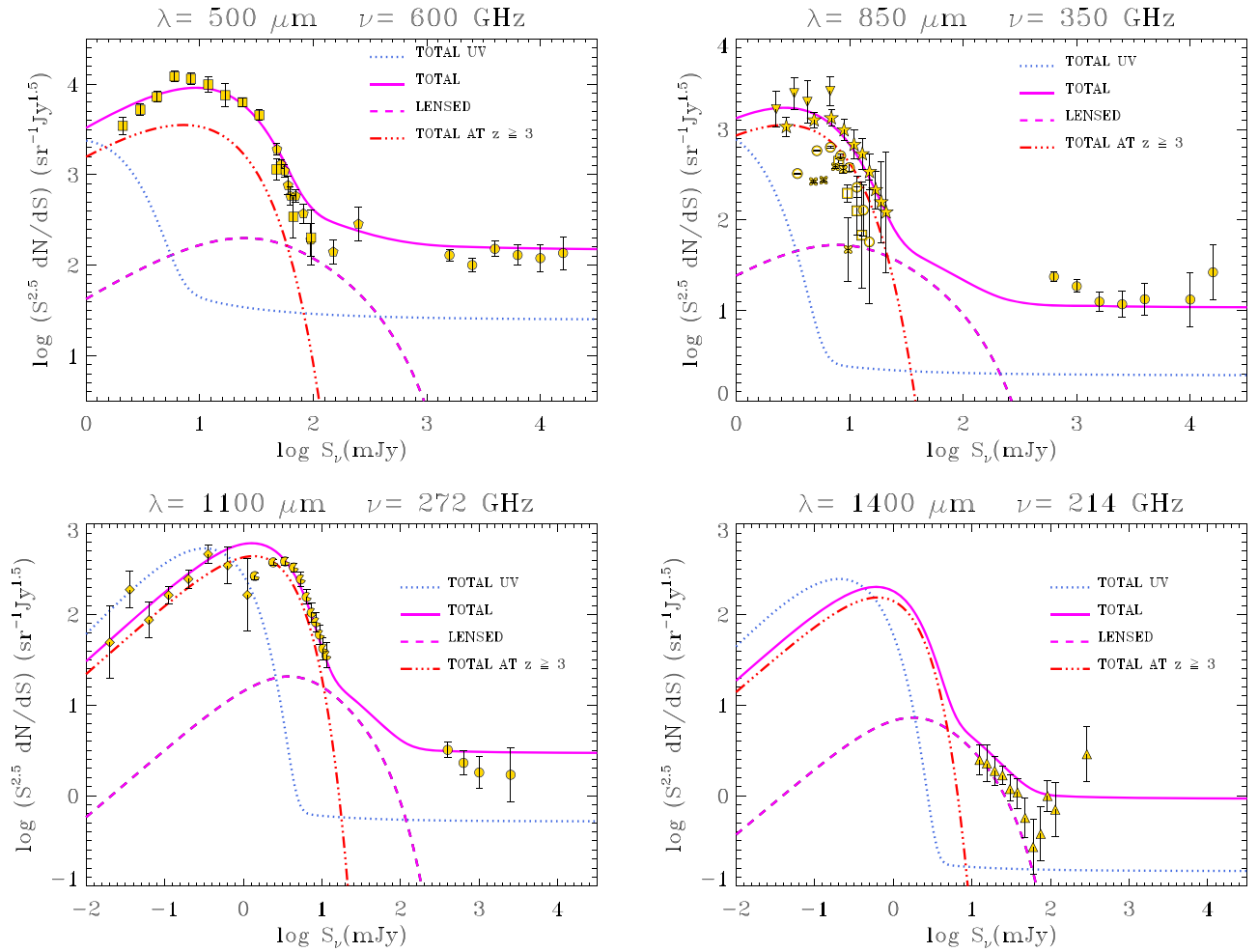

Figure 3. Euclidean-normalized differential number counts at 500 (top left), 850 (top right), 1100 (bottom left), and 1400 μm (bottom right). Magenta lines refer to the counts derived from our intrinsic SFR function; the contribution to the total counts (solid) from strongly lensed galaxies (dashed) is highlighted. The triple dotted–dashed red line is the contribution to unlensed counts from galaxies at $z \gtrsim 3$. The blue dotted line refers to the counts derived from the UV-inferred SFR function. Data (gold symbols) are from Planck Collaboration VII (2013; filled circles), *Herschel*/*HerMES* by Bethérmin et al. (2012; filled squares), *Herschel*/*ATLAS* by Clements et al. (2010; filled pentagons), *SCUBA* by Coppin et al. (2006; filled stars) and Noble et al. (2012; filled reversed triangles), *LABOCA* by Weiss et al. (2009; open circles), *ALMA* by Karim et al. (2013; open clovers), Simpson et al. (2015; open squares), and Fujimoto et al. (2016; filled diamonds), *AzTEC* by Scott et al. (2012; filled pacmans) and *SPT* by Mocanu et al. (2013; filled triangles, where the counts at S > 100 mJy are actually upper limits).

dramatically to less than 10% based on the (dust-corrected) UV-inferred SFR function.

All in all, the agreement with the observed counts, redshift distributions (including lensed sources), and cosmic infrared background constitutes a robust validation of our intrinsic SFR function in a range of SFRs and redshift where the far-IR data on the luminosity function are still not available.

Two remarks are in order. First, we have investigated the impact of using different SEDs typical of star-forming, dust-obscured galaxies, namely, the Cosmic Eyelash (our reference, see above), the average from the ALESS sample (Swinbank et al. 2014; da Cunha et al. 2015; this is similar to the classic SED of Arp 220, see Rangwala et al. 2011), and the local ULIRG+Seyfert1 galaxy Mrk 231 (e.g., Polletta et al. 2007). In Figure 6, we show that the effect on the steep part of the 850 μm counts (mostly contributed by $z \gtrsim$ 2–3) is small when changing from the Eyelash to the ALESS (or Arp 220) SED; the same holds at any $\lambda \gtrsim 500\,\mu$m, since for galaxies at $z \gtrsim$ 2–3 the SEDs are quite similar in the corresponding range of rest-frame wavelengths. On the contrary, considering a SED shape like that of Mrk 231, which exhibits more power in the mid-IR regime, would appreciably underpredict the (sub-) millimeter counts.

Second, we point out that the contribution of active galactic nuclei (AGNs) is marginally relevant to the above statistics. As a matter of fact, the AGN contribution to the IR emission, generally ascribed to the presence of a dusty torus, is characterized by SEDs peaking at 20–40 μm with a rapid fall-off at longer wavelengths because the emission is dominated by hot dust grains. Theoretical works have shown that this fall-off is weakly dependent on the geometry, clumpiness of the torus, and orientation of the line of sight (e.g., Pier & Krolik 1992; Granato & Danese 1994; Efstathiou & Rowan-Robinson 1995; Nenkova et al. 2008). The results of these works well match the observed SEDs of local AGNs.

In Figure 6 (top panel), we present the typical rest-frame SEDs of obscured AGNs (referring to both local and high-z objects) as fit by Siebenmorgen et al. (2015). This plot illustrates the relative contribution of an obscured AGN and of its host dusty galaxy, under the assumption that their integrated luminosity over the range 3–1100 μm is the same (a conservative hypothesis for most (sub-)millimeter-selected

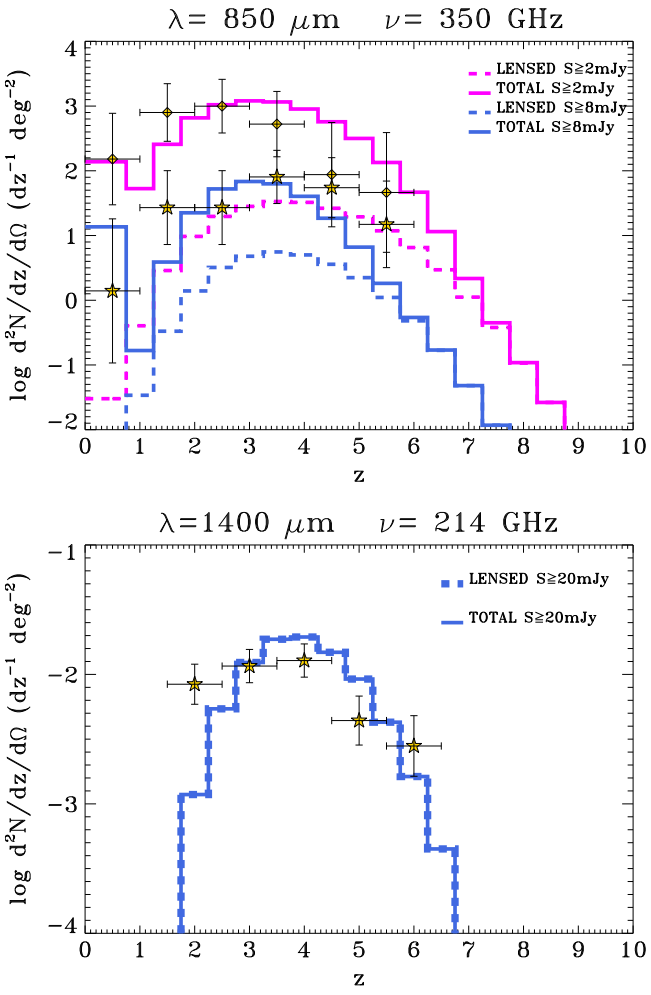

Figure 4. Redshift distributions at 850 (top panel) and 1400 μm (bottom panel). At 850 μm, magenta lines refer to a limiting flux of 2 mJy and blue lines to a limiting flux of 8 mJy, with the contribution to the total (solid) from strong galaxy-scale gravitational lensing (dashed) highlighted; data are from *AzTEC-LABOCA* by Koprowski et al. (2014, stars) and from *SCUBA-2* by Koprowski et al. (2016, diamonds). At 1400 μm blue lines (solid and dashed are superimposed) refer to a limiting flux of 20 mJy; data are from *ALMA-SPT* by Weiss et al. (2013, stars).

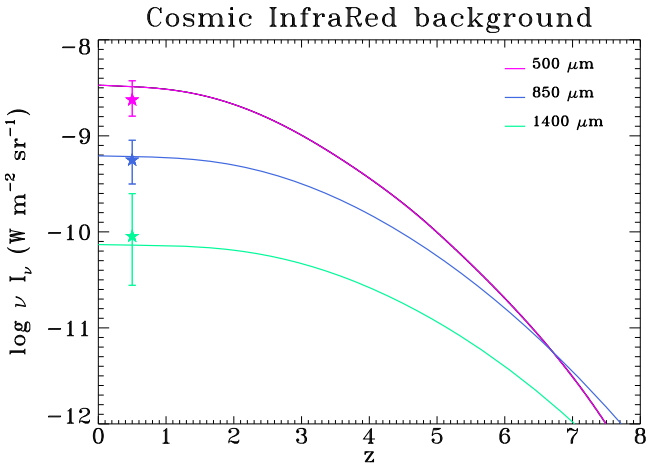

Figure 5. Contribution to the the cosmic infrared background at 500 (magenta), 850 (blue), and 1400 μm (green) from redshift greater than z, as derived from our intrinsic SFR function, compared with the observational determinations at $z \approx 0$ (stars, slightly offset in redshift for clarity) by Fixsen et al. (1998; see also Lagache et al. 1999).

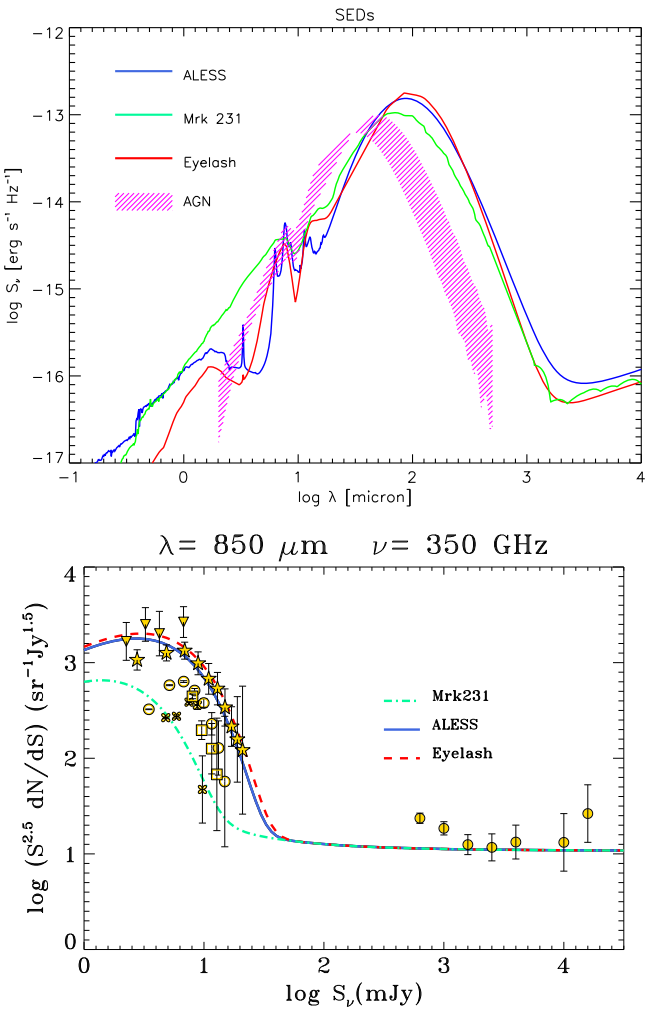

Figure 6. Top panel: comparison among the SEDs of three typical dust-obscured, star-forming galaxies (normalized in the range 3–1100 μm to 1 erg s^{-1}): red line refers to the Cosmic Eyelash (Ivison et al. 2010), blue line to the average from ALESS galaxies (Swinbank et al. 2014; da Cunha et al. 2015), and green line to Mrk 231 (e.g., Polletta et al. 2007). The typical SEDs of obscured AGNs (including both low- and high-z objects) is plotted as a magenta region (Siebenmorgen et al. 2015). Bottom panel: effect of varying the SED on the total 850 μm counts; data points as in Figure 3.

galaxies). In order to test the SFR function at $z \gtrsim 3$, the statistics of counts and lensed objects at $\lambda \sim 1400\,\mu$m (Weiss et al. 2013) are extremely informative. This observational wavelength corresponds to rest-frame $\lambda \gtrsim 200\,\mu$m for galaxies at $z \lesssim 6$. From Figure 6, it is apparent that the obscured AGN flux/luminosity is $\lesssim$10% with respect to that of the host galaxy.

This conclusion is also supported by Delvecchio et al. (2014), who have performed broadband SED decomposition in about 4000 galaxies detected at 160 μm by *Herschel* in the redshift range $z \sim 0$–3. They find that the SEDs of galaxies with an appreciable AGN contribution (around 30% of the total) are well fit by the standard starburst component peaking at $\approx$100 μm and by an AGN component peaking at 20–40 μm (see Figure 5 of Delvecchio et al. 2014). Moreover, the same approach has been exploited by Gruppioni et al. (2015) in the COSMOS and GOODS-S fields of the PEP and *HerMES*/*Herschel* surveys to subtract the AGN emission on an object-by-object basis, and then to reconstruct the bright end of the SFR function at $z \lesssim 3$ (see the hexagons in Figure 1); as a

matter of fact, their outcomes agree with our SFR function, again indicating that the AGN contribution is irrelevant.

Swinbank et al. (2014) and da Cunha et al. (2015) reported observations with *ALMA* of 99 high-z, sub-milimeter galaxies in ECDFS with multi-wavelength observations, covering a very wide spectral range. These authors show that the composite spectrum of such galaxies in the range $\lambda \sim 10$–$1000\ \mu$m can be well represented by the superposition of three gray bodies referring to different dust components, namely, cold, warm, and hot, with temperatures of $T \approx 20$–30 K, 50–60 K, and 80–120 K, respectively. The hot component peaking at around 30 μm suggests the presence, in a statistical sense, of an AGN contribution, which becomes irrelevant at $\lambda \gtrsim 70$–$80\ \mu$m.

All in all, the combination of the short lifetime for luminous AGNs and of their SED makes the AGN component irrelevant as for the far-IR/(sub-)millimeter counts. A general discussion on the luminosity function and counts of AGN types 1, 2, and 3 (the latter being those growing at the center of star-forming galaxies at substantial redshift) at wavelengths ranging from the UV to millimeter bands was presented by Cai et al. (2013). We stress that these findings do not exclude relationships between star formation and the central black hole accretion history (e.g., Alexander & Hickox 2012; Kormendy & Ho 2013; Lapi et al. 2014; Aversa et al. 2015).

2.2. Validating the Intrinsic SFR Function via the Continuity Equation

We now turn to validating our intrinsic SFR function by exploiting the observed stellar mass function at $z \gtrsim 4$. The SFR and stellar mass functions are naturally related via the continuity equation, along the lines already pursued for lower redshifts by Aversa et al. (2015; see also Leja et al. 2015). The continuity equation was originally devised for connecting the AGN statistics to the demographics of both active and dormant supermassive black holes; recently, it has also been applied with remarkable success to link the evolution of the galaxy SFR function $N(\psi, t)$ to the stellar mass functions $N(M_\star, t)$ of active and passively evolving galaxies across cosmic times. We refer the reader to the paper by Aversa et al. (2015) for an extensive discussion of this approach; here, we simply recall its basic features and implement some improvements.

The continuity equation in integral formulation can be written as

$$N(\psi, t) = \int_0^\infty dM_\star\, [\partial_t N(M_\star, t)]\, \frac{d\tau}{d\psi}(\psi|M_\star, t); \qquad (7)$$

here, t is the cosmological time corresponding to redshift z, τ is internal galactic time (i.e., the time elapsed since the triggering of significant star formation), and $d\tau/d\psi$ is the time spent by a galaxy with current stellar mass $M_\star$ in the SFR range $[\psi, \psi + d\psi]$ given a star formation history $\psi = \psi(\tau|M_\star, t)$. Since we are mainly interested in the high-redshift $z \gtrsim 4$ evolution of the mass function, we have neglected any source term due to "dry" merging, i.e., events adding the whole mass content in stars of merging galaxies without contributing significantly to the luminosity associated with star formation.

As for the star formation history $\psi(\tau|M_\star, t)$, Aversa et al. (2015) have considered the standard, time-honored assumptions of a constant, or exponentially increasing/decreasing SFR. Here, we follow the indications emerging from recent studies of SED-modeling (e.g., Papovich et al. 2011; Smit et al. 2012; Moustakas et al. 2013; Steinhardt et al. 2014) for a slow, power-law increase of the SFR with a characteristic time $\tau_\star$, in the form

$$\psi(\tau|M_\star, t) = \psi_\star \left(\frac{\tau}{\tau_\star}\right)^\kappa \qquad \psi_\star = \frac{M_\star(\kappa + 1)}{\tau_\star}, \qquad (8)$$

with $\kappa \approx 0.5$; the second equation above simply links the normalization $\psi_\star$ of the SFR history to the current stellar mass $M_\star$. However, we checked that our results do not depend on this specific representation. The quantity $d\tau/d\psi$ entering the continuity equation reads

$$\frac{d\tau}{d\psi}(\psi|M_\star, t) = \frac{\tau_\star^{1+1/\kappa}}{\kappa} \frac{\psi^{-1+1/\kappa}}{[(1+\kappa)M_\star]^{1/\kappa}} \times \Theta_{\rm H}\left[\psi \leqslant \frac{(1+\kappa)M_\star}{\tau_\star}\right]; \qquad (9)$$

the Heaviside function $\Theta_{\rm H}[\cdot]$ specifies that a galaxy with current mass $M_\star$ cannot have shone at an SFR ψ exceeding $M_\star(\kappa + 1)/\tau_\star$.

At the high redshifts, $z \gtrsim 4$, of interest here, the stellar mass function is dominated by actively star-forming galaxies; thus, we adopt the star formation timescale $\tau_\star$ inferred from the observed main sequence ψ–$M_\star$ (e.g., Rodighiero et al. 2011, 2014; Speagle et al. 2014; Whitaker et al. 2014; Renzini & Peng 2015). Such a timescale $\tau_\star = \tau_\star(\psi, t)$ is itself a function of the SFR/stellar mass and cosmic time.

We exploit the determination of the main sequence by Speagle et al. (2014), which takes into account many samples with different primary selections (UV, optical, far-IR; see their Table 3). This is a good representation of the statistical average relationships between SFR and stellar mass for galaxies over their lifetime (see also Koprowski et al. 2016). Note that in the Speagle et al. determination, "off-main-sequence" galaxies are accounted for by a scatter of 0.3 dex around the median relation, which is in turn dependent on redshift (see also da Cunha et al. 2015; Munoz & Peeples 2015).

We point out that at lower redshifts, $z \lesssim 1.5$, it would be important to take the fraction of passively evolving galaxies into account in order to obtain sound estimates of the relic stellar mass function from the continuity equation (see Aversa et al. 2015; Leja et al. 2015). We also stress that $\tau_\star$ is in general different from the total duration of the star formation episode over which most of the stellar mass is accumulated. In more detail, the two timescales are both quite close to a few 10^8 years for massive galaxies, which typically formed their stars in a violent burst with SFR $\psi \gtrsim 10^2\, M_\odot\, {\rm yr}^{-1}$; however, they can be appreciably different for less massive objects, which typically formed their stars steadily at much lower rates $\psi \lesssim 10\, M_\odot\, {\rm yr}^{-1}$ over several Gyr. Thus, the total burst duration is an inverse function of the stellar mass in agreement with the standard downsizing picture (e.g., Cowie et al. 1996), while the star formation timescale from the main sequence $\psi \propto M_\star^{0.8}$ is a slow, direct function of the stellar mass or of the time-averaged SFR, namely, $\tau_\star \propto M_\star^{0.2} \propto \langle\psi\rangle^{0.25}$. From a physical point of view, the latter dependence reflects the brevity of the condensation/dynamical timescales within the shallower potential wells of smaller-mass halos, which are typically virialized earlier according to the standard structure formation paradigm (see Fan et al. 2010).

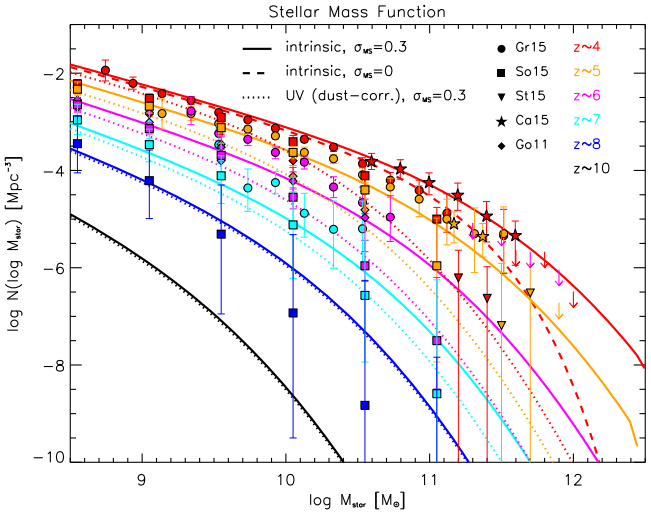

Figure 7. Stellar mass function at redshifts $z \approx 4$–10 (color-coded), obtained via the continuity equation from the intrinsic (solid) or UV-inferred (dotted) SFR function and a scatter of $\sigma_{\rm MS} \approx 0.3$ dex around the median main-sequence relationship; at $z \approx 4$ the outcome from the intrinsic SFR function with $\sigma_{\rm MS} \approx 0$ is highlighted by the dashed red line. Data of the stellar mass functions (see text for details) are from Grazian et al. (2015; circles), Song et al. (2015; squares), Stefanon et al. (2015; inverse triangles), Caputi et al. (2015; stars), and González et al. (2011; diamonds).

The solution of the continuity equation can be worked out using the same method followed in Aversa et al. (2015), to obtain

$$N(\log M_\star, t) = -\kappa(1+\kappa)^{1/\kappa} M_\star^{1/\kappa} \int_0^t dt' \frac{\partial_{\ln\psi}}{f_{\tau_\star}} \times \left[\frac{N(\log\psi, t)\psi^{-1/\kappa}}{\tau_\star^{1+1/\kappa}}\right]_{|\psi=(1+\kappa)M_\star/\tau_\star}, \quad (10)$$

with the shorthand $f_{\tau_\star} \equiv 1 + \partial_{\log\psi}[\log\tau_\star]$; this is a novel result, although we note that the differences in the outcome relative to a constant or exponential SFR are minor. Similarly, the value of the power-law index κ is marginally relevant if varied from the fiducial value $\kappa = 0.5$ within the range from 0 (constant SFR) to 1 (linearly increasing SFR).

In Figure 7, we show the resulting stellar mass function at $z \gtrsim 4$ when using our intrinsic SFR functions as input. The outcome is compared with the determination of the mass function at $z \approx 4$–8 by González et al. (2011), Grazian et al. (2015), Song et al. (2015), and Stefanon et al. (2015). The agreement is particularly good with the near-IR selected samples based on *HST*/WFC3/IR and *Spitzer* data by Grazian et al. (2015; see also Duncan et al. 2014 and Caputi et al. 2015) when the scatter of 0.3 dex around the median main-sequence relation suggested by Speagle et al. (2014) is taken into account.

Note that the stellar mass functions by González et al. (2011) and Song et al. (2015) are instead obtained from UV-selected samples by combining the observed UV luminosity function with the $M_{\rm UV}$–$M_\star$ relationship. Even including a scatter of 0.4 dex in the latter relation as adopted by Song et al. (2015), the stellar mass function is still appreciably lower at the high-mass end with respect to the determination based on near-IR samples; this is due to the underestimation of the luminosity function at the bright end by UV surveys because of insufficient corrections for dust extinction.

We stress that the number density of massive galaxies $M_\star \approx 10^{11}\,M_\odot$ is still quite high at $z \approx 5$, amounting to about $\approx 10^{-5}\,{\rm Mpc}^{-3}$. Then, this value is expected to drop from around $\approx 5 \times 10^{-8}\,{\rm Mpc}^{-3}$ at $z \approx 7$, to $\approx 2 \times 10^{-9}\,{\rm Mpc}^{-3}$ at $z \approx 8$, and to less than $10^{-10}\,{\rm Mpc}^{-3}$ at $z \approx 10$; this is mainly due to the rapid fall-off of the halo mass function at these high redshifts. However, at $z \gtrsim 6$, data are still uncertain, but reliable measurements will become feasible with the next generation of instruments; in particular, the *James Webb Space Telescope* (*JWST*) will allow us to determine stellar masses $M_\star \gtrsim 10^{10}\,M_\odot$ up to $z \sim 7$ (see Caputi 2011). This will eventually allow a detailed validation of the intrinsic SFR function via the continuity equation at these extremely high redshift.

On the other hand, the SFR functions inferred solely from UV data, even corrected for dust extinction, strongly underpredict the observed stellar mass function for $M_\star \gtrsim$ a few $10^{10}\,M_\odot$ at $z \lesssim 5$. This demonstrates that at these redshifts, the strong suppression of the bright end in the UV-inferred SFR function with respect to the intrinsic one must be traced back to star formation in dust-enshrouded environments, and cannot be related to any form of feedback, such as that from supernovae (SNe) or AGNs, which instead would lower the stellar mass. In the redshift range $z \sim 6$–8, the intrinsic SFR function approaches the UV-inferred one, and particularly so at $z \gtrsim 7$ (see Figure 1); as a consequence, the continuity equation implies that the stellar mass functions derived from the intrinsic or UV (dust-corrected) SFR functions are both consistent with the observational determinations within their large uncertainties (see Figure 7).

3. LINKING TO THE HALO MASS VIA ABUNDANCE MATCHING

We now connect the SFR and stellar mass function of active galaxies with the statistics of the underlying, gravitationally dominant DM halos. We exploit the abundance matching technique, a standard method of deriving a monotonic relationship between galaxy and halo properties by matching the corresponding integrated number densities (e.g., Vale & Ostriker 2004; Shankar et al. 2006; Behroozi et al. 2013; Moster et al. 2013).

We derive the relationship $M_\star(M_{\rm H}, z)$ between the current stellar mass $M_\star$ and the halo mass $M_{\rm H}$ by solving the equation (see Aversa et al. 2015 for details)

$$\int_{\log M_\star}^{\infty} d\log M_\star'\, N(\log M_\star', z) = \int_{-\infty}^{+\infty} d\log M_{\rm H}'\, N(\log M_{\rm H}', z) \times \frac{1}{2}\,{\rm erfc}\left\{\frac{\log[M_{\rm H}(M_\star)/M_{\rm H}']}{\sqrt{2}\,\sigma_{\log M_\star}}\right\}, \quad (11)$$

which holds when a lognormal distribution of $M_\star$ at given $M_{\rm H}$ with dispersion $\sigma_{\log M_\star}$ is adopted; we follow previous studies based on the abundance matching technique (see references above) and fiducially adopt $\sigma_{\log M_\star} \approx 0.15$. In Equation (11), the quantity $N(\log M_{\rm H}, z)$ is the galaxy halo mass function, i.e., the mass function of halos hosting one individual galaxy (see Aversa et al. 2015); actually, for $z \gtrsim 4$ and for the halo masses of interest here, it coincides with the standard halo mass

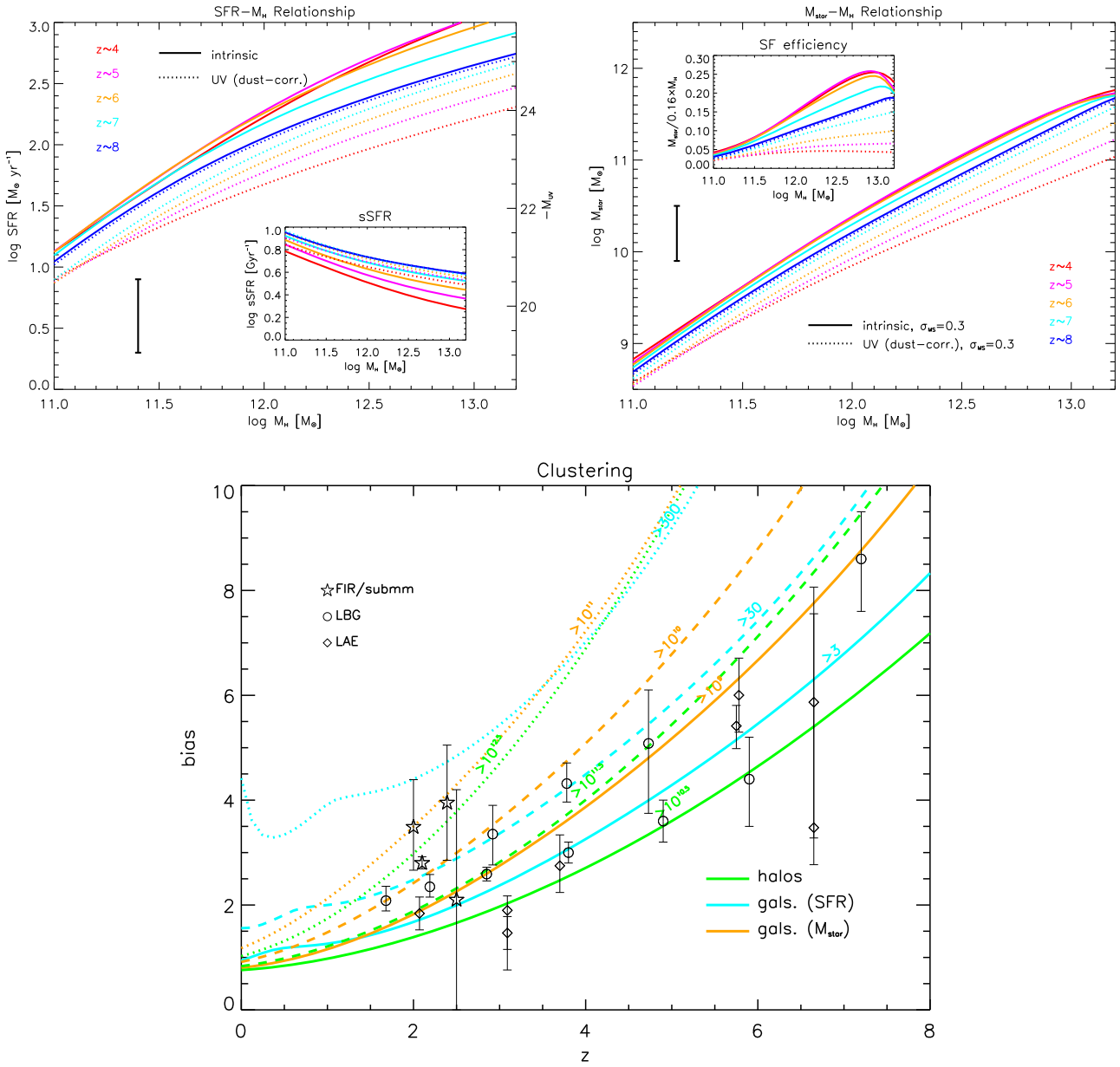

Figure 8. Top left panel: the relationship $\psi - M_{\rm H}$ between SFR (right axis shows the corresponding uncorrected UV magnitude) and host halo mass at different redshift $z \approx 4$–8 (color-code), as derived from the abundance matching of the halo mass function to the intrinsic SFR function (solid lines) or to the SFR function inferred from (dust-corrected) UV data (dotted lines); the inset illustrates the corresponding sSFR $= \psi/M_\star$ vs. the halo mass. Top right panel: the same for the relationship $M_\star$–$M_{\rm H}$ between stellar mass and host halo mass. The inset illustrates the corresponding star formation efficiency, i.e., the stellar to baryon fraction $M_\star/0.16 \times M_{\rm H}$ vs. the halo mass. In both of the top panels, the error bars represent the typical uncertainty. Bottom panel: the evolution with redshift of the clustering bias; results are shown for halos (green) with DM mass exceeding $10^{10.5}$ (solid), $10^{11.5}$ (dashed), and $10^{12.5}$ $M_\odot$ (dotted), for galaxies (cyan) with SFR exceeding 3 (solid), 30 (dashed), and 300 $M_\odot$ yr^{-1} (dotted), and for galaxies (orange) with stellar masses exceeding 10^9 (solid), 10^{10} (dashed), and 10^{11} $M_\odot$ (dotted). Data for FIR/(sub-) millimeter galaxies (stars) are from Weiss et al. (2009), Hickox et al. (2012), Ono et al. (2014), and Bianchini et al. (2015); for LBGs (circles) from Ouchi et al. (2004), Adelberger et al. (2005), Lee et al. (2006), Overzier et al. (2006), Bielby et al. (2013), and Barone-Nugent et al. (2014); and for LAE (diamonds) from Gawiser et al. (2007), Ouchi et al. (2010), and Guaita et al. (2010).

function from cosmological N-body simulations (e.g., Tinker et al. 2008).

The same technique may also be applied to look for a relation $\psi(M_{\rm H}, z)$ specifying the typical SFR ψ in a halo of mass $M_{\rm H}$ at redshift z. However, when dealing with the SFR, one has to take into account that active galaxies shine with a characteristic star formation timescale $\tau_\star(\psi, z)$ which may be smaller than the cosmic time $t(z)$. In practice, one can still rely on Equation (11) by substituting the following: the current stellar mass with the SFR, i.e., $M_\star \to \psi$; the stellar mass function with the SFR function divided by the SFR timescale, i.e., $N(\log M_\star, z) \to N(\log \psi, z)/\tau_\star(\psi, z)$; and the halo mass function with the halo creation rate (see Lapi et al. 2013), i.e., $N(\log M_{\rm H}, z) \to \partial_t^+ N(\log M_{\rm H}, z)$.

In Figure 8 (top panels), we show the resulting $M_\star$–$M_{\rm H}$ and ψ–$M_{\rm H}$ relationships. Note that these relationships refer to active star-forming galaxies, while Aversa et al. (2015) have presented the corresponding outcomes for the total population

including objects in passive evolution; as expected, for active galaxies the SFR at a given halo mass is higher.

The most remarkable feature of these relationships is the little or no evolution with redshift at given $M_{\rm H}$; this clearly indicates that the star formation in galaxies at high redshift $z \gtrsim 4$ is regulated by similar, in situ processes (Moster et al. 2013; Aversa et al. 2015), and not by merging or gas infall from cosmological scales. The insets illustrate the sSFR $= \psi/M_\star$ and the star formation efficiency, i.e., the current stellar to baryon ratio $M_\star/0.16 \times M_{\rm H}$, as a function of $M_{\rm H}$.

The latter highlights that star formation in galaxies is an extremely inefficient process, i.e., only a small amount of the available baryon content of a halo is converted into stars. From a physical point of view, this is usually interpreted in terms of competition between cooling and heating processes. In low-mass halos, heating is provided by energy feedback from SN explosions, which regulate star formation at slow rates $\psi \lesssim 10\,M_\odot\,{\rm yr}^{-1}$ over timescales of several Gyr. In massive halos, cooling rates are not significantly offset by SN feedback, yielding the well-known overcooling problem (Cirasuolo et al. 2005; for a recent discussion see Dutton et al. 2015). This motivated a number of authors (Granato et al. 2004; Di Matteo et al. 2005; Lapi et al. 2006, 2014) to propose that star formation can proceed at much higher levels $\psi \gtrsim 30\,M_\odot\,{\rm yr}^{-1}$ over several 10^8 years, until the central AGN attains enough power to shine as a quasar, quenching the SFR abruptly and sweeping away most of the gas and dust content (e.g., Shankar et al. 2006; Aversa et al. 2015). On the contrary, neglecting quasar feedback in large halos would produce stellar masses well above the observed values.

We stress that the abundance matching relationships derived on the basis of the intrinsic and UV-inferred SFR function differ, marginally at $z \gtrsim 7$ but considerably at $z \approx 4$. It is extremely important to take such differences into account for a proper interpretation of the observational data in terms of galaxy formation scenarios. For example, consider a galaxy with a stellar mass of $M_\star \approx 10^{11}\,M_\odot$ at $z \approx 5$, whose number density is of the order of $\approx 10^{-5}\,{\rm Mpc}^{-3}$ (see Duncan et al. 2014; Grazian et al. 2015). From the $M_\star$–$M_{\rm H}$ relationship (see Figure 8, top right), the host halo is seen to feature a mass of $M_{\rm H} \approx$ a few $10^{12}\,M_\odot$. Moreover, according to the ψ–$M_{\rm H}$ relationship with its 0.3 dex scatter (see Figure 8, top left), the SFR turns out to be $\psi \approx 500$–$1000\ M_\odot\,{\rm yr}^{-1}$ when based on the intrinsic SFR function, but only of the order of $\psi_{\rm UV} \approx 50$–$100\,M_\odot\,{\rm yr}^{-1}$ when relying on the UV-inferred one; the corresponding SFR timescales $M_\star/\psi$ amounts to $\approx 10^8$ years and 10^9 years, respectively. Given that the age of the universe at $z \approx 5$ is of the order of 1.2 Gyr, the UV-inferred solution would require star formation to occur well in advance of the initial halo virialization, and/or extreme assumptions on the star formation efficiency or halo occupation (Steinhardt et al. 2015). On the other hand, the solution based on the intrinsic SFR function yields a formation redshift of the host halos $z_{\rm form} \approx 5.4$; the corresponding halo number density for $M_{\rm H} \approx$ a few $10^{12}\,M_\odot$ reads $\sim 10^{-5}\,{\rm Mpc}^{-3}$, in agreement with the stellar mass functions observed at $z \approx 5$ for $M_\star \approx 10^{11}\,M_\odot$ where the argument started.

The abundance matching relationships are also fundamental to interpreting the clustering signal associated with high-z dusty galaxies (see Figure 8, bottom panel). Specifically, we find that at $z \approx 4$–5, galaxies endowed with SFR $\psi \gtrsim 100$–$300\,M_\odot\,{\rm yr}^{-1}$ and $M_\star \gtrsim 10^{11}\,M_\odot$ are typically hosted within halos of $M_{\rm H} \gtrsim$ a few $10^{12}\,M_\odot$, which are extremely biased and clustered. We note that on the basis of the observed clustering signal, Hildebrandt et al. (2009) and Bian et al. (2013) instead associate the same halo masses with galaxies selected with UV magnitudes $M_{\rm UV} \lesssim -21$; when using the dust correction based on the UV slope, they estimate a corresponding SFR $\psi \approx 30$–$50\,M_\odot\,{\rm yr}^{-1}$. This low value of the intrinsic SFR is underestimated because of an incomplete dust correction applied to UV-selected samples (see Figure 8, top left panel), and would again raise an issue on the star formation timescale (see above; Steinhardt et al. 2015).

From the top panels of Figure 8, it is apparent that when abundance matching is performed by exploiting the intrinsic SFR function, the evolution with redshift of the SFR and stellar mass at fixed halo mass is small and well within the errors determined by observations. On the other hand, the evolution is amplified when abundance matching is performed by exploiting the (dust-corrected) UV-inferred SFR function. The latter case would imply an increasing star formation efficiency with redshift, which is reminiscent of the claim by Finkelstein et al. (2015b). On the contrary, we find no evolution (within errors) of star formation efficiency when based on the intrinsic SFR function.

4. HUNTING HIGH-z DUSTY STAR-FORMING GALAXIES

Above, we have stressed the relevance of probing the statistics of galaxies at $z \sim 4$–6 with SFRs $\psi \gtrsim 10^2\,M_\odot\,{\rm yr}^{-1}$, which contribute substantially to the high-mass end of the stellar mass function. Since most of these galaxies with high SFRs are likely dust-enshrouded, exploiting IR data is mandatory to fully assess the intrinsic SFR function. How to achieve this goal in practice, given the current and upcoming observational facilities in the far-IR/(sub-)millimeter and/or UV band, constitutes the issue addressed below.

4.1. Selecting Dusty Galaxies in the Far-IR/(Sub-) Millimeter Band

As a starting point, in Figure 9 (top panel), we illustrate the redshift evolution for our reference SED (see Section 2.1). The SED has been normalized so that the far-IR emission in the range 3–1100 μm corresponds to an SFR of $\psi \approx 1\,M_\odot\,{\rm yr}^{-1}$.

We have illustrated the positions on the SED of the observational wavelengths for various instruments of interest here: 250, 350, and 500 μm for the SPIRE instrument on board *Herschel*; 450 and 850 μm for the *SCUBA-2* instrument at the James Clerk Maxwell telescope; ~1100 μm for *AzTEC* at the LMT; 1400 μm for *SPT*; and 850, 1400, and 3000 μm for *ALMA*. We have also highlighted the 5σ detection limits for such instruments (attained in the deepest large-scale surveys undertaken so far or in the near future): $S_{250} \approx 35$ mJy, $S_{350} \approx 40$ mJy, and $S_{500} \approx 50$ mJy for SPIRE; $S_{450} \approx 8$ mJy and $S_{850} \approx 2$ mJy for *SCUBA-2*; $S_{1100} \approx 1$ mJy for *AzTEC*; $S_{1400} \approx 20$ mJy for *SPT*; and $S_{850} \approx 0.42$, $S_{1400} \approx 0.11$, and $S_{3000} \approx 0.02$ mJy for *ALMA* (500 hr on 100 arcmin^2).

The accurate determination of the spectroscopic redshift for a large sample of dusty galaxies is a major problem. In order to probe the bright end of the SFR function at $z \gtrsim 3$, a strategy could be to preselect high-redshift sources using flux/color criteria from surveys conducted with *Herschel* or *SCUBA-2*, and then perform a more accurate photometric (or even

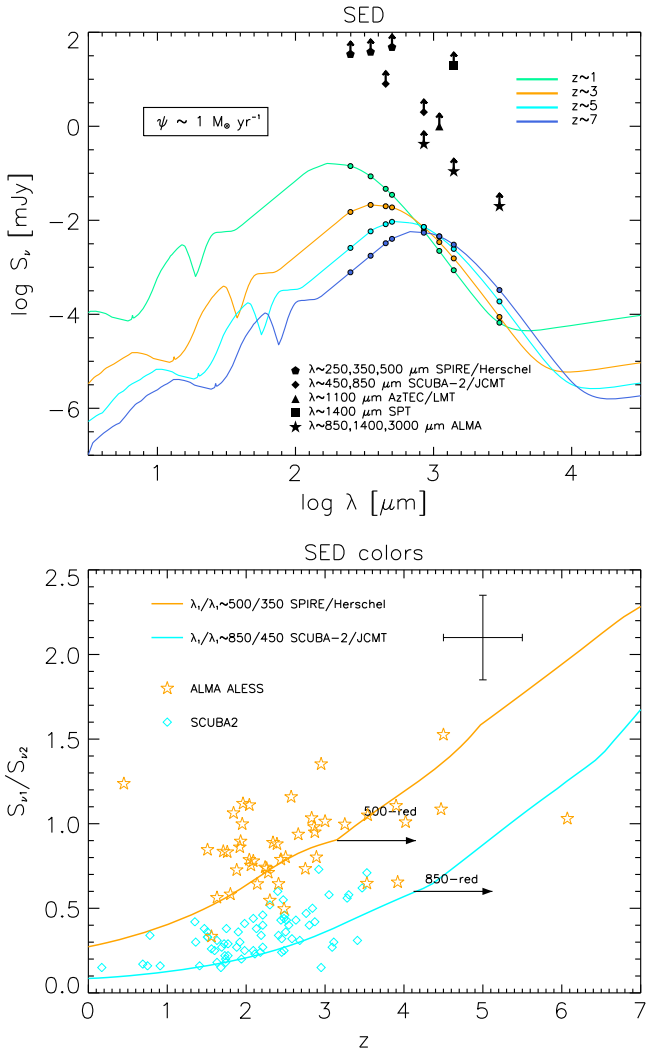

Figure 9. Top panel: the SED of a typical high-z, dust-obscured star-forming galaxy located at redshift $z \approx 1$ (green), 3 (orange), 5 (cyan), and 7 (blue), normalized to a SFR $\psi = 1\,M_{\odot}\,\mathrm{yr}^{-1}$ in the range $\lambda \approx 3$–$1100\,\mu$m. Colored symbols illustrate the values of the SED at different operating wavelengths for various instruments: SPIRE/*Herschel* (circles), *SCUBA-2* (diamonds), *AzTEC* (triangles), *SPT* (squares), and *ALMA* (stars). The corresponding 5σ sensitivities are shown by the black symbols with arrows. Bottom panel: SED colors $S_{\nu,1}/S_{\nu,2}$ as a function of redshift, exploited for *Herschel* and *SCUBA-2* preselection of dusty galaxies; different lines refer to 500/350 (orange) and 850/450 (cyan) colors. Arrows indicate the redshift ranges where red galaxies are preferentially located. Data are from *ALMA*/ALESS by Swinbank et al. (2014; orange stars) and from *SCUBA-2* by Koprowski et al. (2016; cyan diamonds); in the upper right corner, the typical data uncertainty on the median is reported.

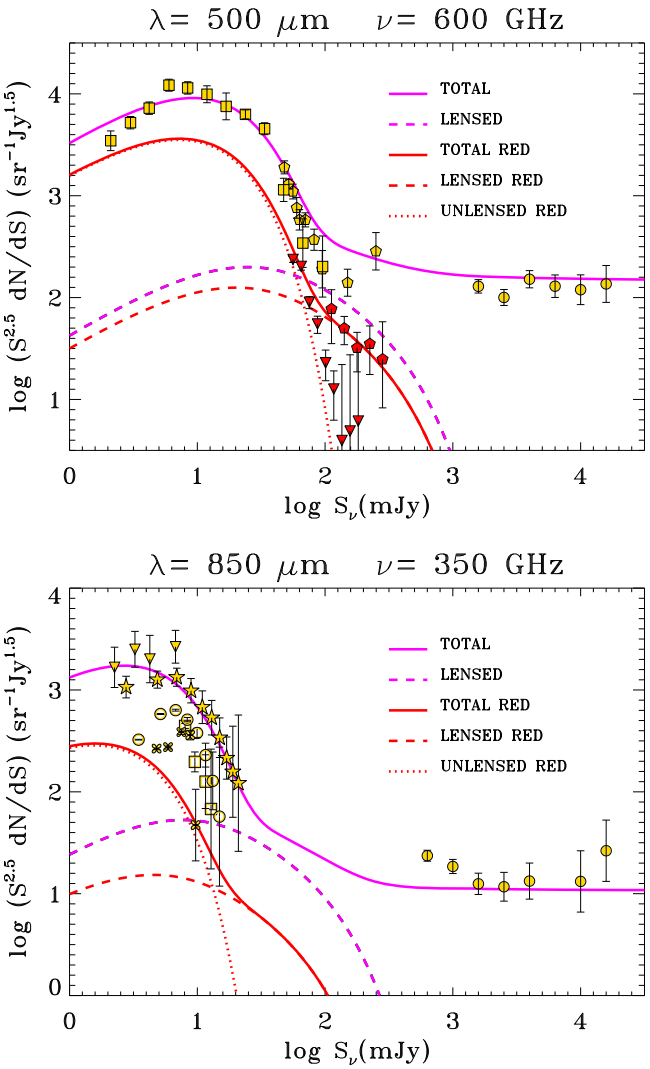

Figure 10. Euclidean-normalized differential number counts at 500 (top) and 850 μm (bottom). Magenta lines refer to the counts derived from our intrinsic SFR function; the contribution to the total counts (solid) from strongly lensed galaxies (dashed) is highlighted. The counts of red galaxies are illustrated in red, with the solid lines referring to the total, the dotted lines to unlensed counts, and the dashed lines to the gravitationally lensed sources. Data (gold symbols) are as in Figure 3. At 500 μm, the data for red galaxies are from *Herschel*/*HerMES* by Asboth et al. (2016, red inverse triangles; see also Dowell et al. 2014) and of candidate high-z lenses from *Herschel*/*ATLAS* by M. Negrello et al. (2016, in preparation, red pentagons; see also Wardlow et al. 2013; Nayyeri et al. 2016).

spectroscopic) redshift determination with observations on source by, e.g., *AzTEC* and *ALMA*.

Commonly used preselection criteria (e.g., Dowell et al. 2014; Asboth et al. 2016) for high-redshift sources based on *Herschel* photometry involve looking for "350-peakers," which are defined as sources with $S_{350}/S_{250} \gtrsim 1$ and $S_{500}/S_{350} \lesssim 1$, or "500-risers," which are defined as sources with $S_{350}/S_{250} \gtrsim 1$ and $S_{500}/S_{350} \gtrsim 1$. Actually, the uncertainties in the flux measurements make the distinction between peakers and risers quite loose; moreover, at $z \gtrsim 4$, the channel at 250 μm refers to rest-frame wavelengths $\lambda \lesssim 50\,\mu$m, where details of the SED due to different dust properties and a possible contribution from an AGN component can be relevant. Thus, here, we mainly focus on the color S_{500}/S_{350}. In Figure 9 (bottom panel), we plot its evolution with redshift and compare it with the measurements from *ALMA*/ALESS by Swinbank et al. (2014), finding reasonable agreement within the large uncertainties. Sources with $S_{500}/S_{350} \gtrsim 0.8$ are high-redshift $z \gtrsim 3$ candidates.

However, the rather high limiting fluxes of *Herschel* cannot probe the SFR function much above $z \sim 5$, since even sources with SFR $\psi \gtrsim 10^3\,M_{\odot}\,\mathrm{yr}^{-1}$ are too faint to be detected. To go much beyond $z \gtrsim 4$, the preselection based on the color S_{850}/S_{450} from *SCUBA-2* photometry is much more efficient. In Figure 9 (bottom panel), we plot its evolution with redshift and compare it with the measurements from *SCUBA-2* by Koprowski et al. (2016), again finding reasonable agreement.

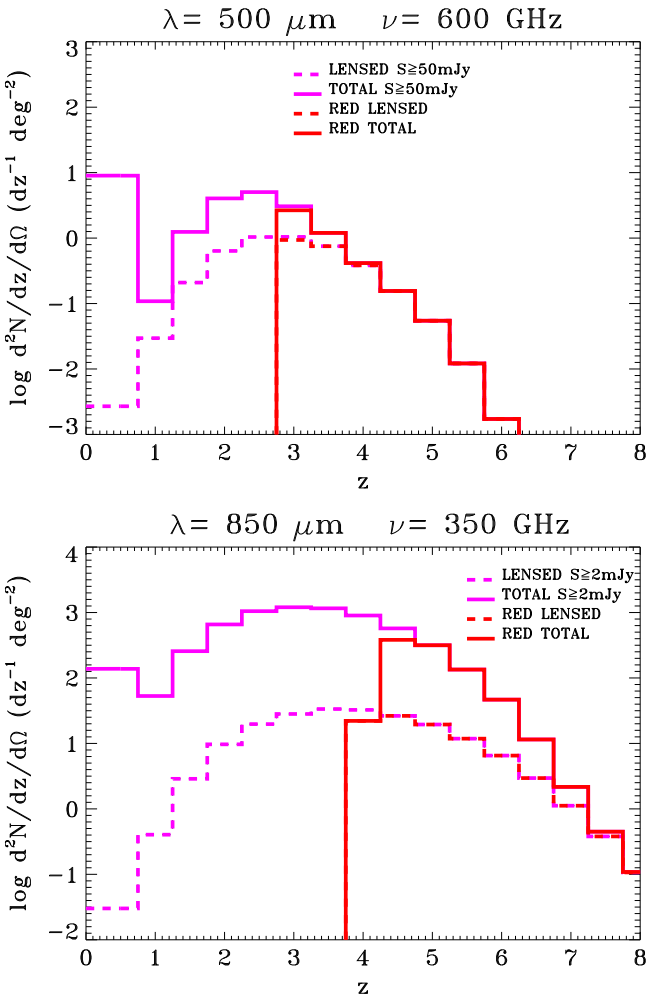

Figure 11. Redshift distributions at 500 (top panel) and 850 μm (bottom panel). At 500 μm, magenta lines refer to the *Herschel* limiting flux of $\approx$50 mJy, with the contribution to the total (solid) from strong galaxy-scale gravitational lensing (dashed) highlighted; the same for red sources is shown in red. At 850 μm, the magenta lines refer to a limiting flux of 2 mJy (again red lines refer to red sources).

It can be seen that the color condition $S_{850}/S_{450} \gtrsim 0.6$ can be exploited to preselect candidate galaxies at $z \gtrsim 4$.

In Figure 10, we show our predictions for the differential counts at 500 and 850 μm for the red sources preselected according to the color criteria discussed above. At 500 μm, the counts of unlensed red sources with $S_{500} \lesssim 100$ mJy agree with the determination by Asboth et al. (2016; see also Dowell et al. 2014), while those of lensed red sources compare well with the candidate lenses in the *Herschel*/*ATLAS* survey selected via their red colors by M. Negrello et al. (2016, in preparation; see also Nayyeri et al. 2016 and Wardlow et al. 2013 for analogous studies in the *Herschel*-HeLMS +HerS and *Herschel*–*HerMES* surveys).

In Figure 11 (top panels), we present the corresponding redshift distributions. At 500 μm (top left), the red high-z candidates are mostly located at redshift $z \gtrsim 3$, featuring SFRs $\psi \gtrsim 300\,M_\odot\,\mathrm{yr}^{-1}$. Interestingly, strong gravitational lensing by foreground galaxies broadens the tail of their redshift distribution toward $z \approx 5$–6; we stress that most of the lensed sources are amplified by relatively modest factors $\langle\mu\rangle \approx 2$–5, so that they still would on average feature SFRs of $\psi \gtrsim 100\,M_\odot\,\mathrm{yr}^{-1}$. At 850 μm (top right), the color selection based on the 850–450 flux ratio picks up objects at $z \gtrsim 4$, with a tail extending out to $z \approx 7$–8. Since the *Herschel* surveys at 350 and 500 μm cover an overall area of $\sim$1000 deg^{-2}, their data can be mined to pick out $\gtrsim$1000 gravitationally lensed galaxies (see González-Nuevo et al. 2012), which, in addition to their cosmological interest (e.g., Eales 2015), can also be used to estimate the SFR distribution function up to $z \sim 6$.

Once the high-z candidates have been preselected, the photometric data from *Herschel* or *SCUBA-2* then have to be supplemented with observations at longer wavelengths from, e.g., *AzTEC* and *ALMA*; the latter instrument can also be exploited to go for a spectroscopic redshift determination, but this plainly requires more observing time, and preferentially a precise estimate of the photometric redshift to choose the most-suited observational band.

4.2. Dusty Galaxies are Not Lost in the UV Band

In the above, we have demonstrated that the intrinsic SFR functions as validated via the (sub-)millimeter counts and the continuity equation are largely underestimated by UV data, especially at the bright end for $z \lesssim 7$. However, next, we show that such dusty galaxies can be efficiently probed by combining current UV surveys with upcoming far-IR/(sub-)millimeter and radio observations.

As a starting point, in Figure 12 (top panel), we present the UV luminosity functions at $z \gtrsim 4$, as reconstructed from the intrinsic SFR function by using various prescriptions for dust extinction. We start by showing that the outcome when no correction is applied considerably overestimates the UV luminosity function for any redshift $z \lesssim 7$ at the bright end $M_{\mathrm{UV}} \lesssim -19$. This occurs even when the standard correction based on the β_{UV}–IRX relation is adopted. This is because, as shown by several authors (e.g., Reddy et al. 2012; Davies et al. 2013; Fan et al. 2014; Coppin et al. 2015), thanks to mid-/far-IR observations of UV-selected galaxies at redshift $z \sim$ 2–4, the attenuation values of galaxies with observed UV magnitude $M_{\mathrm{UV}} \lesssim -21$ are strongly in excess with respect to those estimated based on the β_{UV}–IRX relation, and feature a very large dispersion. The standard interpretation is that star formation occurs preferentially within heavily dust-enshrouded molecular clouds, while the UV slope mainly reflects the emission from stars obscured by the diffuse, cirrus dust component (see Silva et al. 1998; Coppin et al. 2015; Reddy et al. 2015). We note that on approaching $z \approx 8$, the β–IRX-corrected luminosity function converges toward the unextincted one, at least down to $M_{\mathrm{UV}} \gtrsim -21.5$, which corresponds to an intrinsic SFR of $\psi \lesssim 30\,M_\odot\,\mathrm{yr}^{-1}$; this suggests that for these galaxies, the timescale required to accumulate a substantial amount of dust becomes longer than their age.

All in all, for $z \lesssim 7$ and $M_{\mathrm{UV}} \lesssim -19$, an attenuation larger than that derived on the basis of the β–IRX relation is needed to recover the UV luminosity function from the intrinsic SFR function.

Observationally, at $z \sim 2$, the the UV attenuation A_{UV} is found to directly correlate with the SFR, although with a large dispersion of about 1 mag (or 0.4 dex in log IRX; e.g., Reddy et al. 2010); the attenuations are already significant, with values of $A_{\mathrm{UV}} \approx 1.5$–2.5 mag (or IRX values of $\approx$4–7) for SFRs $\psi \approx 30$–$50\,M_\odot\,\mathrm{yr}^{-1}$. A heuristic rendition of such an observed correlation for $\psi \gtrsim 30\,M_\odot\,\mathrm{yr}^{-1}$ reads

$$A_{\mathrm{UV}} = \psi^{0.25}. \quad (12)$$

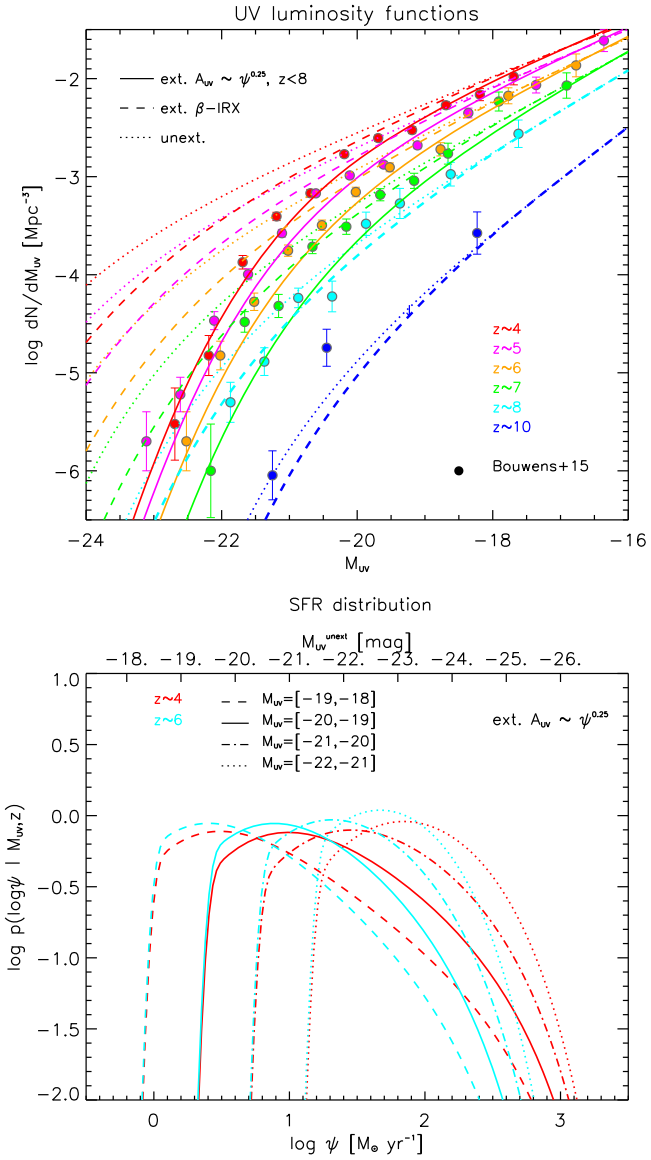

Figure 12. Top panel: UV luminosity function at different redshift $z \approx 4$–10 (color-coded), as reconstructed from our intrinsic SFR function by not correcting for dust extinction (dotted lines), correcting via the standard $\beta_{\rm UV}$–IRX relation (dashed lines), and via the simple relationship $A_{\rm UV} = \psi^{0.25}$ (solid lines) with a scatter of 1 mag at given ψ (for $z < 8$). Data points (circles) are from Bouwens et al. (2015). Bottom panel: normalized SFR distribution of galaxies in the observed UV magnitude bins centered at $M_{\rm UV} \approx -18.5$ (dashed lines), -19.5 (solid), -20.5 (dotted–dashed), and -21.5 (dotted) at redshifts $z \sim 4$ (red) and 6 (cyan). The upper axis refers to the unextincted UV magnitude $M_{\rm UV}^{\rm unext}$ associated with the intrinsic SFR ψ. The extinction law $A_{\rm UV} = \psi^{0.25}$ with a scatter of 1 mag at given ψ has been adopted.

Note that, via a stacking analysis of 850 μm emission from Lyman Break Galaxies in the *SCUBA-2* Cosmology Legacy Survey, Coppin et al. (2015; see their Table 2) find at $z \sim 3$–5 average values of SFR $\psi \approx 70$–$130\,M_\odot\,{\rm yr}^{-1}$ and UV attenuations of $A_{\rm UV} \approx 2.3$–2.5, which are broadly consistent with Equation (12). Note that the relation expressed by Equation (12) represents an average UV attenuation defined as $A_{\rm UV} \equiv 2.5\log(1 + L_{\rm IR}/L_{\rm UV})$ in terms of the integrated UV and IR luminosities, and as such it is a basic quantity whose estimate does not require a full radiative transfer approach (e.g., Meurer et al. 1999; Reddy et al. 2015).

In Figure 12 (top panel), we show this to map remarkably well the intrinsic SFR functions onto the observed UV luminosity function over the redshift range $z \approx 4$–7. The outcome for the luminosity function is mostly sensitive to the scatter of the above relation; the behavior at the bright end of the luminosity function constrains it to be within ± 0.2 of the best-fit value of 1 mag. We note the caveat that the above equation does not include a dependence on metallicity Z, which may well affect the dust abundance. As a matter of fact, Reddy et al. (2010) find a direct dependence between $A_{\rm UV}$ and the metallicity Z, with the former becoming appreciable when $Z \gtrsim Z_\odot/3$. A combined dependence $A_{\rm UV} \propto \psi^\alpha\, Z^\beta$ including both the SFR and metallicity has been considered by Mao et al. (2007) and Cai et al. (2014) based on the $M_{\rm UV}$ versus $E(B-V)$ relation by Shapley et al. (2001) and the UV luminosity functions at a different redshift. Actually, in their approach, $\psi(\tau)$, $Z(\tau)$, and hence $A_{\rm UV}(\tau)$, are functions of the galactic age τ, but for galaxies with quite robust SFR $\psi \gtrsim 30$–$50\,M_\odot\,{\rm yr}^{-1}$, the SFR is roughly constant and the metallicity saturates rapidly for $\tau \gtrsim$ a few 10^7 years to slightly subsolar values; all in all, their time-averaged relation is very close to Equation (12).

In Figure 12 (bottom panel), we represent the SFR distribution (areas under curves are normalized to 1) for galaxies selected with a given observed UV magnitude at redshift $z \sim 4$–6; the upper axis refers to the unextincted UV magnitude corresponding to a given SFR ψ. Plainly, the rapid truncation of the distributions to the left of the peak occurs because SFR values yielding an unexctincted UV magnitude fainter than that observed are not allowed ($A_{\rm UV} > 0$ must hold). The decrease of the distributions to the right of the peak reflects the convolution between the intrinsic SFR function and the adopted attenuation law with its large dispersion. The distributions tend to be narrower at higher redshift and for brighter observed UV magnitudes, due to the evolution of the intrinsic SFR function at the high-SFR end, and to the decrease of the extinction with increasing redshift.

Based on the star formation main sequence, we expect that most of the dusty galaxies with intrinsic SFR $\psi \gtrsim 100\,M_\odot\,{\rm yr}^{-1}$ which appear as faint UV objects with $M_{\rm UV} \gtrsim -21$ also feature large stellar masses $M_\star \gtrsim$ a few $10^{10}\,M_\odot$. As such, they appear as upper outliers in the $M_\star$–$M_{\rm UV}$ diagram (see Duncan et al. 2014; Coppin et al. 2015; Grazian et al. 2015; Song et al. 2015). Note that a similar location could also be occupied by almost passively evolving galaxies, but their number at $z \gtrsim 4$ is expected to be small, since the star formation timescales implied by the main sequence are close to the age of the universe. As a consequence, a significant fraction of the outliers are expected to be highly star-forming, massive galaxies, and as such constitute particularly well-suited targets for far-IR and (sub-)millimter observations. At redshift $z \gtrsim 6$, the same regime will be explored by *JWST*.

The broad shape of the SFR distributions implies that dusty, strongly star-forming galaxies with $\psi \gtrsim 30\,M_\odot\,{\rm yr}^{-1}$ are not lost in the UV, but rather are moved by their strong attenuation $A_{\rm UV} \gtrsim 2.3$ at fainter magnitudes; although they are outnumbered by the intrinsically faint and poorly attenuated galaxies, they can nevertheless be singled out following the strategy proposed below. In Table 2, we present the number per square arcmin of dusty, UV-selected galaxies expected per observed magnitude bin, for a given threshold in SFR. The numbers decrease quite rapidly with increasing redshift and increasing SFR threshold.

Table 2
Number of Dusty, UV-selected Galaxies (in arcmin^{-2})

$M_{\rm UV}$	$\psi \gtrsim 100\,M_\odot$ yr^{-1}				$\psi \gtrsim 300\,M_\odot$ yr^{-1}				$\psi \gtrsim 1000\,M_\odot$ yr^{-1}			
Observed	$z=3$	$z=4$	$z=5$	$z=6$	$z=3$	$z=4$	$z=5$	$z=6$	$z=3$	$z=4$	$z=5$	$z=6$
−17	0.14	0.09	0.04	0.01	0.03	0.02	0.006	0.0006	0.002	0.0008	0.00008	0.000001
−18	0.28	0.18	0.08	0.02	0.06	0.03	0.009	0.001	0.005	0.002	0.0002	0.000003
−19	0.28	0.18	0.08	0.02	0.06	0.03	0.009	0.001	0.005	0.002	0.0002	0.000003
−20	0.24	0.16	0.07	0.02	0.05	0.03	0.008	0.001	0.004	0.001	0.0001	0.000002
−21	0.12	0.08	0.03	0.01	0.03	0.01	0.004	0.0006	0.002	0.0006	0.00006	0.000001
−22	0.03	0.02	0.007	0.002	0.006	0.003	0.001	0.0001	0.0003	0.0001	0.00001	0.0000002

Note. For more details, see Section 4.2 and Figure 12.

For example, considering that the current areas surveyed in the UV amount to $\approx 10^3$ arcmin^2 (see Bouwens et al. 2015; their Table 1), the expected numbers are around several hundreds of galaxies with SFR $\psi \gtrsim 100\,M_\odot\,{\rm yr}^{-1}$ at $M_{\rm UV} \lesssim -17$ and $z \approx 4$; this number decreases to several tens at $z \approx 6$ for $\psi \gtrsim 100\,M_\odot\,{\rm yr}^{-1}$, and to a hundred at $z \approx 4$ for $\psi \gtrsim 300\,M_\odot\,{\rm yr}^{-1}$.

These UV data could be exploited in combination with (sub-)millimeter and/or radio observations to reconstruct the bright end of the intrinsic SFR function (e.g., Barger et al. 2014). The strategy involves observing the areas $\lesssim 10^3$ arcmin^2 of current UV surveys (see Bouwens et al. 2015) in the (sub-)millimeter and/or radio band. On one hand, this will allow us to measure unbiased the intrinsic SFR of strongly dust-obscured galaxies from (sub-)millimeter/radio data; on the other hand, the cross matching with the positions from the UV maps will allow us to associate with these galaxies reliable UV photometric redshifts. Note that the combination with UV photometric data will also help in removing from (sub-)millimeter and radio observations any contamination from low-luminosity, unobscured AGNs and low-z star-forming galaxies.

Specifically, given the areas covered by current or upcoming UV surveys (Bouwens et al. 2015), in Figure 13, we present the required sensitivity to detect at least 30 objects (to obtain sound statistics) with a given SFR threshold in a redshift bin of width $\Delta z \approx 1$. In particular, we focus on SFR $\psi \gtrsim 100$ and $1000\,M_\odot\,{\rm yr}^{-1}$, and consider three wavelengths: 850 and 1400 μm of interest for *ALMA*, and 21 cm (1.4 GHz) of interest for *SKA*. The dots refer to redshift bins centered around $z \sim 1$, 3, 5, and 7, with the redshift increasing following the small colored arrows. The upward black arrows illustrate the 5σ sensitivity limits of *ALMA* and *SKA*, for a total integration time of 500 hr, on survey areas of 100, 1000, and 10,000 arcmin^2 (from left to right). Here, we have adopted as reference the following specifications: for *ALMA* (in survey-mode configuration, see http://www.ioa.s.u-tokyo.ac.jp/~ytamura/Wiki/?plugin=attach&refer=ALMA&openfile=tamura-almawg-060302.pdf) at 850–1400 μm, a field of view (FOV) of 0.02–0.04 arcmin^2 and a 5σ sensitivity of 0.1–0.05 mJy hr$^{-1/2}$; for *SKA* (configuration *SKA1-MID*; see Prandoni & Seymour 2015) at 21 cm (1.4 GHz), a FOV of about 0.35 deg^2 and a 5σ sensitivity of 0.01 mJy hr$^{-1/2}$.

It can be seen that for 100 arcmin^2, which can be easily covered by the subfields of current UV surveys, both *ALMA* and *SKA* can detect tens of galaxies at $z \approx 4$–6 with SFRs $\psi \gtrsim 100\,M_\odot\,{\rm yr}^{-1}$; on the other hand, for 1000 arcmin^2, the widest area currently surveyed in the UV is needed to statistically sample galaxies with SFRs $\psi \gtrsim 300\,M_\odot\,{\rm yr}^{-1}$; finally, an area of 10,000 arcmin^2, as possibly surveyed by the future *LSST* (e.g., Ivezic et al. 2008), will enable us to detect an appreciable

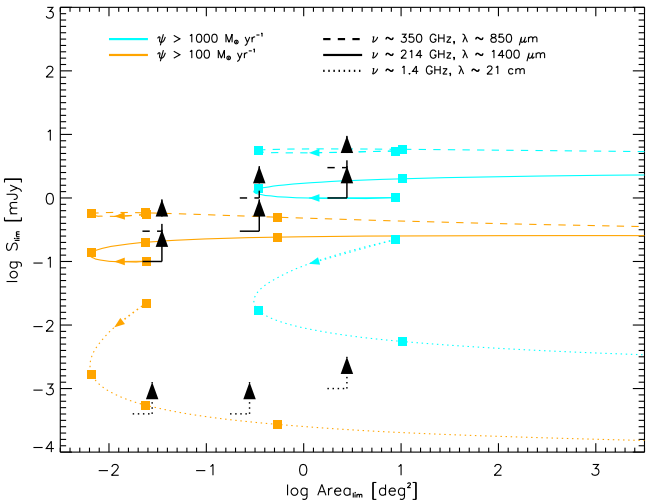

Figure 13. Diagram showing the limiting flux and the area of a (sub-) millimeter and radio survey required to detect at least 30 dusty galaxies per redshift bin $\Delta z \approx 1$. Results are shown for two different thresholds in intrinsic SFR $\psi \gtrsim 100$ (orange lines) and $\gtrsim 1000\,M_\odot\,{\rm yr}^{-1}$ (cyan lines) at three wavelengths: 850 (dashed) and 1400 μm (solid) of interest for *ALMA*, and 21 cm (1.4 GHz, dotted) of interest for *SKA*. Along each curve, the redshift increases following the small colored arrows, with the dots referring to $z \approx 1$, 3, 5, and 7. The black upward arrows illustrate the *ALMA* and *SKA* 5σ sensitivity limits (500 hr of integration time, see the text for details) for surveys on 100, 1000, and 10,000 arcmin^2.

number of dusty galaxies with SFRs $\psi \gtrsim 1000\,M_\odot\,{\rm yr}^{-1}$. Note that at the flux limits and on the survey areas considered here, gravitational lensing is only marginally effective, even at wavelengths $\lambda \gtrsim 1$ mm where its effect on the counts is most relevant. For example, from Figure 3 (bottom right panel), it can be seen that at 1.4 mm for fluxes of 1 mJy, the lensed sources are only a small fraction around a few percent of the total population.

On the (sub-)millimeter side, another interesting instrument that could be exploited for these observations is *NIKA2*; we adopt as reference specifications (see http://ipag.osug.fr/nika2/Instrument.html) at 1.2 mm a FOV of about 40 arcmin^2 and a 5σ sensitivity around 1.3 mJy hr$^{-1/2}$. Then, in 500 hr, it can attain a 5σ sensitivity of 0.1 mJy on 100 arcmin^2, of 0.3 mJy on 1000 arcmin^2, and of 1 mJy on 10,000 arcmin^2; thus, *NIKA2* at 1.2 mm will perform similarly to *ALMA* at 1.4 mm. On the radio side, the *SKA* precursor *MeerKAT* is also interesting; we adopt as reference specifications (see Prandoni & Seymour 2015) at 21 cm (1.4 GHz) a FOV of about 0.8 deg^2 and a 5σ sensitivity around 0.01 mJy hr$^{-1/2}$. In 500 hr, it can attain a 5σ sensitivity of 0.5 μJy on 100 arcmin^2, of 0.5 μJy on 1000 arcmin^2, and of 0.8 μJy on 10,000 arcmin^2; thus, it will

perform similarly to *SKA*. However, we note that *NIKA2* and *MeerKAT*, as opposed to *ALMA* and *SKA*, in the surveys considered above would work close to their confusion limit. Such instruments feature resolution around 10 and 5 arcsec, respectively; these imply, upon considering the shape of the counts (see Figure 3), a confusion limit of around 0.1 mJy for *NIKA2* at 1.2 mm, and at the μJy level for *MeerKAT* at 21 cm (1.4 GHz).

In summary, surveying common areas in the UV as well as in the (sub-)millimeter and/or radio bands looks to be a most promising strategy for characterizing the SFR function at the bright end $\psi \gtrsim 100\,M_{\odot}\,\mathrm{yr}^{-1}$ up to $z \lesssim 8$.

5. SUMMARY AND CONCLUSIONS

The history of star formation in massive galaxies (the host of high-redshift quasars) is a fundamental problem in galaxy evolution. In the present paper, we address two important issues. Is star formation in galaxies mainly regulated by in situ processes or by merging? How does the presence of dust affect the statistics of the SFR in galaxies at high redshift $z \gtrsim 3$?

To cast light on these issues, we have designed a method (see Section 2) to build the intrinsic SFR function at different redshifts up to $z \lesssim 10$. Specifically, at $z \lesssim 3$, we have fit a Schechter function to the UV data for SFRs $\psi \lesssim 30\,M_{\odot}\,\mathrm{yr}^{-1}$ and to the far-IR data for SFRs $\psi \gtrsim 100\,M_{\odot}\,\mathrm{yr}^{-1}$. We have further imposed that at $z \gtrsim 8$, the UV-inferred SFR function is representative of the intrinsic one, since we expect small attenuation by dust due to the short age of the universe. This allows us to set the redshift evolution of the Schechter parameters, and hence to work out specific predictions for the SFR functions over the full range $z \sim 0$–10.

We have found that for $z \lesssim 7$, the UV-inferred SFR function, even when corrected for dust absorption according to the standard prescriptions based on the UV slope, strongly underestimate the intrinsic SFR function for SFRs $\psi \gtrsim 30\,M_{\odot}\ \mathrm{yr}^{-1}$. Thus, our result on the SFR function implies the existence of a galaxy population at $z \gtrsim 4$ featuring large star formation rates SFR $\psi \gtrsim 10^{2}\,M_{\odot}\,\mathrm{yr}^{-1}$ in heavily dust-obscured conditions. These galaxies constitute the high-redshift counterparts of the dusty star-forming population already surveyed for $z \lesssim 3$ in the far-IR band by the *Herschel Space Observatory*. A number of these objects have been discovered thanks to spectroscopic follow-up of high-redshift candidates identified in UV or IR surveys, and their corresponding number densities are well reproduced by our intrinsic SFR function. We have further validated the latter by comparison with the observed (sub-)millimeter counts, redshift distributions, and cosmic infrared background (see Section 2.1), finding excellent agreement.

We have exploited the continuity equation approach and the "main-sequence" star formation timescales to show that our intrinsic SFR function is fully consistent with the stellar mass function of active, star-forming galaxies observed at redshift $z \gtrsim 4$ (see Section 2.2). In particular, we reproduce the considerable abundance of galaxies with stellar masses in excess of a few $10^{10}\,M_{\odot}$ at redshift $z \gtrsim 4$, and even their still substantial number densities out to $z \sim 6$. On the contrary, we show that the UV-inferred SFR function would produce a strong deficit of galaxies with such large stellar masses.

We have computed the average relationships between intrinsic SFR and stellar mass versus halo mass via the abundance matching technique (see Section 3). We find that such relationships show little if any evolution with redshift at given M_{H}; this clearly indicates that star formation in galaxies at high redshift $z \gtrsim 4$ is regulated by similar in situ processes, and not by merging or gas infall from cosmological scales. We have pointed out that our results on the intrinsic SFR functions straightforwardly overcome the "impossibly early galaxy problem" recently pointed out by Steinhardt et al. (2015).

In order to probe the bright end of the SFR functions at $z \gtrsim 4$, we have computed the expected galaxy number counts and redshift distributions (including galaxy-scale gravitational lensing) of dusty star-forming galaxies. We have also designed an observational strategy (see Section 4) to hunt these galaxies based on a preselection in the far-IR or (sub-)millimeter band with *Herschel* and *SCUBA-2*, possibly supplemented by on-source observations with millimeter instruments like *AzTEC* and *ALMA*, aimed at recovering photometric (or even spectroscopic) redshifts (see Section 4.1).

We have investigated (see Section 4.2) the nature of the UV-selected galaxies at $z \gtrsim 4$, finding that their attenuation properties are strongly in excess of those routinely estimated from the UV slope, i.e., via the β_{UV}–IRX correlation. This is because star formation preferentially occurs within molecular clouds, i.e., cocooned environments that are extremely rich in dust; on the other hand, the UV slope mostly refers to the milder attenuation of the emission from relatively older stars by the diffuse cirrus dust component. We have shown that a simple, power-law representation of the UV attenuation due to molecular clouds in terms of the SFR maps the intrinsic SFR function onto the observed UV luminosity function.

We have shown that dusty, strongly star-forming galaxies with $\psi \gtrsim 30\,M_{\odot}\,\mathrm{yr}^{-1}$ are not lost in the UV, but rather are moved by their strong attenuation $A_{\mathrm{UV}} \gtrsim 2.3$ at fainter magnitudes, where they are outnumbered by the intrinsically faint and poorly attenuated galaxies. Such highly star-forming, dust-obscured and massive galaxies are expected to be located on the high side of the M_{UV}–$M_{\star}$ relationship; as such, these constitute particularly suitable targets for far-IR and (sub-) millimeter observations with current instruments, and for near/mid-IR observations with the *JWST*.

We have also discussed (see Section 4.2) how the intrinsic SFR function at high redshift could be probed by combining current UV surveys with observations from (sub-)millimeter instruments like *ALMA* and *NIKA2*, and upcoming radio facilities like *SKA* and its precursors.

In conclusion, we stress that collecting large statistics of UV and far-IR selected galaxies at high redshift is extremely informative on timescales for dust production and destruction. For instance, in the case of AZTEC-3 at $z \approx 5.3$ (Riechers et al. 2014) and HLFS3 at $z \approx 6.3$ (Cooray et al. 2014), far-IR data indicate SFRs $\psi \sim 1000\,M_{\odot}\,\mathrm{yr}^{-1}$, stellar masses $M_{\star} \sim 1$–$5 \times 10^{10}\,M_{\odot}$, and dust masses $M_{d} \sim 3 \times 10^{8}\,M_{\odot}$. The star formation timescale $\tau_{\star} = M_{\star}/\psi \sim 1$–$5 \times 10^{7}$ years implies that a large amount of dust has been rapidly accumulated in these galaxies; adopting a Chabrier IMF and no dust destruction, for type-II SN explosion, a dust mass yield of $m_{d} \sim 0.7$–$3\,M_{\odot}$ per SN is required. This yield is somewhat higher than the value found for SN 1987A $m_{d} \sim 0.8\,M_{\odot}$ per SN, which may be an upper bound (Matsuura et al. 2015).

On the other hand, the SN-driven shock waves destroy dust grains on a timescale of $\tau_{D} = \tau_{\mathrm{SN}}\,M_{\mathrm{ISM}}/m_{g}$, where τ_{SN} is the time between SN explosions, M_{ISM} is the mass of the ISM (gas and dust), and m_{g} is the mass of ISM cleared per SN explosion

(e.g., Slavin et al. 2015). For the Milky Way, $\tau_{\rm SN} \sim 125$ years, $M_{\rm ISM} \sim 5 \times 10^9\,M_\odot$, and $m_g \sim 600\,M_\odot$ hold, to yield $\tau_D \sim$ Gyr. On the contrary, for the high-z galaxies mentioned above, the extremely large SFRs $\psi \sim 1000\,M_\odot\,{\rm yr}^{-1}$ imply $\tau_{\rm SN} \sim 0.1$ year, making $\tau_D \lesssim 10^7$ years so short with respect to $\tau_\star$ as to exclude that destruction can be neglected. Additional stellar sources of dust may be at work, such as W-R stars, AGB stars, and SNe I; the first are minor dust producers, while the second and the third can form significant dust amounts but over long timescales $\gtrsim$ a few $\times 10^8$. Note that even accretion in molecular clouds can have an important role in dust formation (for a review, see Dwek & Cherchneff 2010).

These instances demonstrate that the issues of dust formation in high-z galaxies and of dust production by SN II and AGB stars are still open problems (see, e.g., the discussion in Dwek & Cherchneff 2011; Dwek et al. 2015; Mancini et al. 2015; Wesson et al. 2015; Michalowski 2015). Large statistical samples of dusty star-forming galaxies at $z \gtrsim 4$ will constitute key data sets for understanding the role of the physical processes involved in dust formation and destruction.

We acknowledge the referee for useful suggestions and comments. We thank Z.-Y. Cai, G. De Zotti, G. Rodighiero, and F. Shankar for helpful discussions, and M. Negrello and S. Eales for having shared with us their data on the counts of color-selected, candidate lensed galaxies from the *Herschel*/*ATLAS* survey before publication. Work financially supported from PRIN INAF 2012 "Looking into the dust-obscured phase of galaxy formation through cosmic zoom lenses in the *Herschel* Astrophysical Large Area Survey" and from PRIN INAF 2014 "Probing the AGN/galaxy co-evolution through ultra-deep and ultra-high-resolution radio surveys." J.G.N. acknowledges financial support from the Spanish MINECO for a "Ramon y Cajal" fellowship.

REFERENCES

Adelberger, K. L., Steidel, C. C., Pettini, M., et al. 2005, ApJ, 619, 697
Alavi, A., Siana, B., Richard, J., et al. 2014, ApJ, 780, 143
Alexander, D. M., & Hickox, R. C. 2012, NewAR, 56, 93
Asboth, V., Conley, A., Sayers, J., et al. 2016, MNRAS, submitted, (arXiv:1601.02665)
Aversa, R., Lapi, A., de Zotti, G., Shankar, F., & Danese, L. 2015, ApJ, 810, 74
Barger, A. J., Cowie, L. L., Chen, C.-C., et al. 2014, ApJ, 784, 9
Barone-Nugent, R. L., Trenti, M., Wyithe, J. S. B., et al. 2014, ApJ, 793, 17
Behroozi, P. S., Wechsler, R. H., & Conroy, C. 2013, ApJ, 770, 57
Béthermin, M., Le Floc'h, E., Ilbert, O., et al. 2012, A&A, 542, A58
Bian, F., Fan, X., Jiang, L., et al. 2013, ApJ, 774, 28
Bianchini, F., Bielewicz, P., Lapi, A., et al. 2015, ApJ, 802, 64
Bielby, R., Hill, M. D., Shanks, T., et al. 2013, MNRAS, 430, 425
Bolton, J. S., Haehnelt, M. G., Warren, S. J., et al. 2011, MNRAS, 416, L70
Bonato, M., Negrello, M., Cai, Z.-Y., et al. 2014, MNRAS, 438, 2547
Bouwens, R. J., Illingworth, G. D., Franx, M., et al. 2009, ApJ, 705, 936
Bouwens, R. J., Illingworth, G. D., Oesch, P. A., et al. 2014, ApJ, 793, 115
Bouwens, R. J., Illingworth, G. D., Oesch, P. A., et al. 2015, ApJ, 803, 34
Bowler, R. A. A., Dunlop, J. S., McLure, R. J., et al. 2015, MNRAS, 452, 1817
Cai, Z.-Y., Lapi, A., Bressan, A., et al. 2014, ApJ, 785, 65
Cai, Z.-Y., Lapi, A., Xia, J.-Q., et al. 2013, ApJ, 768, 21
Caputi, K. I. 2011, in Frontier Science with the James Webb Space Telescope, see http://realserver4v.stsci.edu/t/data/2011/06/2611/KarinaCaputi.pdf
Caputi, K. I., Ilbert, O., Laigle, C., et al. 2015, ApJ, 810, 73
Carilli, C. L., Riechers, D., Walter, F., et al. 2013, ApJ, 763, 120
Casey, C. M., Narayanan, D., & Cooray, A. 2014, PhR, 541, 45
Chabrier, G. 2003, PASP, 115, 763
Chapman, S. C., Scott, D., Steidel, C. C., et al. 2000, MNRAS, 319, 318
Cirasuolo, M., Shankar, F., Granato, G. L., De Zotti, G., & Danese, L. 2005, ApJ, 629, 816
Clemens, M. S., Negrello, M., de Zotti, G., et al. 2013, MNRAS, 433, 695
Clements, D. L., Rigby, E., Maddox, S., et al. 2010, A&A, 518, L8
Conroy, C. 2013, ARA&A, 51, 393
Cooray, A., Calanog, J., Wardlow, J. L., et al. 2014, ApJ, 790, 40
Coppin, K., Chapin, E. L., Mortier, A. M. J., et al. 2006, MNRAS, 372, 1621
Coppin, K. E. K., Geach, J. E., Almaini, O., et al. 2015, MNRAS, 446, 1293
Cowie, L. L., Songaila, A., Hu, E. M., & Cohen, J. G. 1996, AJ, 112, 839
Cucciati, O., Tresse, L., Ilbert, O., et al. 2012, A&A, 539, A31
da Cunha, E., Walter, F., Smail, I. R., et al. 2015, ApJ, 806, 110
Davies, L. J. M., Bremer, M. N., Stanway, E. R., & Lehnert, M. D. 2013, MNRAS, 433, 2588
Delvecchio, I., Gruppioni, C., Pozzi, F., et al. 2014, MNRAS, 439, 2736
Di Matteo, T., Springel, V., & Hernquist, L. 2005, Natur, 433, 604
Dowell, C. D., Conley, A., Glenn, J., et al. 2014, ApJ, 780, 75
Duncan, K., Conselice, C. J., Mortlock, A., et al. 2014, MNRAS, 444, 2960
Dutton, A. A., Macció, A., Stinson, G. S., et al. 2015, MNRAS, 453, 2447
Dwek, E., & Cherchneff, I. 2010, in AIP Conf. Proc. 1294, The First Stars and Galaxies: Challenges for the Next Decade, ed. D. J. Whalen, V. Bromm, & N. Yoshida (San Francisco, CA: ASP), 142
Dwek, E., & Cherchneff, I. 2011, ApJ, 727, 63
Dwek, E., Staguhn, J., Arendt, R. G., et al. 2015, ApJ, 813, 119
Eales, S. A. 2015, MNRAS, 446, 3224
Efstathiou, A., & Rowan-Robinson, M. 1995, MNRAS, 273, 649
Fan, L., Lapi, A., Bressan, A., et al. 2010, ApJ, 718, 1460
Fan, L.-L., Lapi, A., Bressan, A., et al. 2014, RAA, 14, 15
Finkelstein, S. L., Papovich, C., Dickinson, M., et al. 2013, Natur, 502, 524
Finkelstein, S. L., Ryan, R. E., Jr., Papovich, C., et al. 2015a, ApJ, 810, 71
Finkelstein, S. L., Song, M., Behroozi, P., et al. 2015b, ApJ, 814, 95
Fixsen, D. J., Dwek, E., Mather, J. C., Bennett, C. L., & Shafer, R. A. 1998, ApJ, 508, 123
Fujimoto, S., Ouchi, M., Ono, Y., et al. 2016, ApJS, 222, 1
Gawiser, E., Francke, H., Lai, K., et al. 2007, ApJ, 671, 278
Goldader, J. D., Meurer, G., Heckman, T. M., et al. 2002, ApJ, 568, 651
González, V., Labbé, I., Bouwens, R. J., et al. 2011, ApJL, 735, L34
González-Nuevo, J., Lapi, A., Fleuren, S., et al. 2012, ApJ, 749, 65
Granato, G. L., & Danese, L. 1994, MNRAS, 268, 235
Granato, G. L., De Zotti, G., Silva, L., Bressan, A., & Danese, L. 2004, ApJ, 600, 580
Grazian, A., Fontana, A., Santini, P., et al. 2015, A&A, 575, A96
Gruppioni, C., Calura, F., Pozzi, F., et al. 2015, MNRAS, 451, 3419
Gruppioni, C., Pozzi, F., Rodighiero, G., et al. 2013, MNRAS, 432, 23
Guaita, L., Gawiser, E., Padilla, N., et al. 2010, ApJ, 714, 255
Hao, C.-N., Kennicutt, R. C. m., Johnson, B. D., et al. 2011, ApJ, 741, 124
Hickox, R. C., Wardlow, J. L., Smail, I., et al. 2012, MNRAS, 421, 284
Hildebrandt, H., Pielorz, J., Erben, T., et al. 2009, A&A, 498, 725
Howell, J. H., Armus, L., Mazzarella, J. M., et al. 2010, ApJ, 715, 572
Ivezic, Z., Tyson, J. A., Abel, B., et al. 2008, arXiv:0805.2366
Ivison, R. J., Swinbank, A. M., Swinyard, B., et al. 2010, A&A, 518, L35
Karim, A., Swinbank, A. M., Hodge, J. A., et al. 2013, MNRAS, 432, 2
Kennicutt, R. C., & Evans, N. J. 2012, ARA&A, 50, 531
Koprowski, M., Dunlop, J. S., Michalowski, M. J., et al. 2016, MNRAS, 458, 4321
Koprowski, M. P., Dunlop, J. S., Michalowski, M. J., Cirasuolo, M., & Bowler, R. A. A. 2014, MNRAS, 444, 117
Kormendy, J., & Ho, L. C. 2013, ARA&A, 51, 511
Lagache, G., Abergel, A., Boulanger, F., Desert, F. X., & Puget, J.-L. 1999, A&A, 344, 322
Lapi, A., & Danese, L. 2015, JCAP, 9, 3
Lapi, A., Gonzalez-Nuevo, J., Fan, L., et al. 2011, ApJ, 742, 24
Lapi, A., Negrello, M., Gonzalez-Nuevo, J., et al. 2012, ApJ, 755, 46
Lapi, A., Raimundo, S., Aversa, R., et al. 2014, ApJ, 782, 69
Lapi, A., Salucci, P., & Danese, L. 2013, ApJ, 772, 85
Lapi, A., Shankar, F., Mao, J., et al. 2006, ApJ, 650, 42
Lee, K.-S., Alberts, S., Atlee, D., et al. 2012, ApJL, 758, L31
Lee, K.-S., Giavalisco, M., Gnedin, O. Y., et al. 2006, ApJ, 642, 63
Leja, J., van Dokkum, P. G., Franx, M., & Whitaker, K. E. 2015, ApJ, 798, 115
Ly, C., Lee, J. C., Dale, D. A., et al. 2011, ApJ, 726, 109
Madau, P., & Dickinson, M. 2014, ARA&A, 52, 415
Magnelli, B., Popesso, P., Berta, S., et al. 2013, A&A, 553, A132
Mancini, M., Schneider, R., Graziani, L., et al. 2015, MNRAS, 451, L70
Mancuso, C., Lapi, A., Cai, Z.-Y., et al. 2015, ApJ, 810, 72
Mao, J., Lapi, A., Granato, G. L., de Zotti, G., & Danese, L. 2007, ApJ, 667, 655
Matsuura, M., Dwek, E., Barlow, M. J., et al. 2015, ApJ, 800, 50
Meurer, G. R., Heckman, T. M., & Calzetti, D. 1999, ApJ, 521, 64
Michalowski, M. J. 2015, A&A, 577, A80

Mocanu, L. M., Crawford, T. M., Vieira, J. D., et al. 2013, ApJ, 779, 61
Moster, B. P., Naab, T., & White, S. D. M. 2013, MNRAS, 428, 3121
Moustakas, J., Coil, A. L., Aird, J., et al. 2013, ApJ, 767, 50
Munoz, J. A., & Peeples, M. S. 2015, MNRAS, 448, 1430
Nayyeri, H., Keele, M., Cooray, A., et al. 2016, MNRAS, submitted (arXiv:1601.03401)
Nenkova, M., Sirocky, M. M., Nikutta, R., Ivezic, Z., & Elitzur, M. 2008, ApJ, 685, 160
Noble, A. G., Webb, T. M. A., Ellingson, E., et al. 2012, MNRAS, 419, 1983
Oesch, P. A., Bouwens, R. J., Carollo, C. M., et al. 2010, ApJL, 725, L150
Oesch, P. A., van Dokkum, P. G., Illingworth, G. D., et al. 2015, ApJL, 804, L30
Ono, Y., Ouchi, M., Kurono, Y., & Momose, R. 2014, ApJ, 795, 5
Ono, Y., Ouchi, M., Mobasher, B., et al. 2012, ApJ, 744, 83
Ouchi, M., Ellis, R., Ono, Y., et al. 2013, ApJ, 778, 102
Ouchi, M., Shimasaku, K., Furusawa, H., et al. 2010, ApJ, 723, 869
Ouchi, M., Shimasaku, K., Okamura, S., et al. 2004, ApJ, 611, 685
Overzier, R. A., Bouwens, R. J., Illingworth, G. D., & Franx, M. 2006, ApJL, 648, L5
Papovich, C., Finkelstein, S. L., Ferguson, H. C., Lotz, J. M., & Giavalisco, M. 2011, MNRAS, 412, 1123
Pier, E. A., & Krolik, J. H. 1992, ApJ, 401, 99
Planck Collaboration VII 2013, A&A, 550, A133
Planck Collaboration XIII 2015, A&A, in press (arXiv:150201589)
Planck Collaboration XVIII 2011, A&A, 536, A18
Planck Collaboration XXX 2014, A&A, 571, A30
Polletta, M., Tajer, M., Maraschi, L., et al. 2007, ApJ, 663, 81
Prandoni, I., & Seymour, N. 2015, POS, AASKA14, 67
Rangwala, N., Maloney, P. R., Glenn, J., et al. 2011, ApJ, 743, 94
Reddy, N., Dickinson, M., Elbaz, D., et al. 2012, ApJ, 744, 154
Reddy, N. A., Erb, D. K., Pettini, M., Steidel, C. C., & Shapley, A. E. 2010, ApJ, 712, 1070
Reddy, N. A., Kriek, M., Shapley, A. E., et al. 2015, ApJ, 806, 259
Reddy, N. A., & Steidel, C. C. 2009, ApJ, 692, 778
Renzini, A., & Peng, Y.-J. 2015, ApJL, 801, L29
Riechers, D. A., Carilli, C. L., Capak, P. L., et al. 2014, ApJ, 796, 84
Roberts-Borsani, G. W., Bouwens, R. J., Oesch, P. A., et al. 2015, ApJ, submitted (arXiv:1506.00854)
Robertson, B. E., Ellis, R. S., Furlanetto, S. R., & Dunlop, J. S. 2015, ApJL, 802, L19
Rodighiero, G., Daddi, E., Baronchelli, I., et al. 2011, ApJL, 739, L40
Rodighiero, G., Renzini, A., Daddi, E., et al. 2014, MNRAS, 443, 19
Rowlands, K., Dunne, L., Dye, S., et al. 2014, MNRAS, 441, 1017
Salmon, B., Papovich, C., Finkelstein, S. L., et al. 2015, ApJ, 799, 183
Schady, P., Savaglio, S., Müller, T., et al. 2014, A&A, 570, A52
Schmidt, M. 1968, ApJ, 151, 393
Scott, K. S., Wilson, G. W., Aretxaga, I., et al. 2012, MNRAS, 423, 575
Shankar, F., Lapi, A., Salucci, P., de Zotti, G., & Danese, L. 2006, ApJ, 643, 14
Shapley, A. E., Steidel, C. C., Adelberger, K. L., et al. 2001, ApJ, 562, 95
Siebenmorgen, R., Heymann, F., & Efstathiou, A. 2015, A&A, 583, A120
Silva, L., Granato, G. L., Bressan, A., & Danese, L. 1998, ApJ, 509, 103
Simpson, J. M., Smail, I., Swinbank, A. M., et al. 2015, ApJ, 807, 128
Slavin, J. D., Dwek, E., & Jones, A. P. 2015, ApJ, 803, 7
Smit, R., Bouwens, R. J., Franx, M., et al. 2012, ApJ, 756, 14
Smith, D. J. B., Dunne, L., da Cunha, E., et al. 2012, MNRAS, 427, 703
Smolcic, V., Aravena, M., Navarrete, F., et al. 2012, A&A, 548, A4
Sobral, D., Smail, I., Best, P. N., et al. 2013, MNRAS, 428, 1128
Song, M., Finkelstein, S. L., Ashby, M. L. N., et al. 2015, ApJ, submitted (arXiv:1507.05636)
Speagle, J. S., Steinhardt, C. L., Capak, P. L., & Silverman, J. 2014, ApJS, 214, 15
Stark, D. P., Ellis, R. S., Bunker, A., et al. 2009, ApJ, 697, 1493
Stefanon, M., Marchesini, D., Muzzin, A., et al. 2015, ApJ, 803, 11
Steinhardt, C. L., Capak, P., Masters, D., & Speagle, J. S. 2015, ApJ, submitted (arXiv:1506.01377)
Steinhardt, C. L., Speagle, J. S., & Capak, P. 2014, ApJL, 791, L25
Strandet, M. L., Weiss, A., Vieira, J. D., et al. 2016, ApJ, submitted (arXiv:1603.05094)
Swinbank, A. M., Simpson, J. M., Smail, I., et al. 2014, MNRAS, 438, 1267
Swinbank, A. M., Smail, I., Longmore, S., et al. 2010, Natur, 464, 733
Tinker, J. L., Kravtsov, A. V., Klypin, A., et al. 2008, ApJ, 688, 709
Vale, A., & Ostriker, J. P. 2004, MNRAS, 353, 189
van der Burg, R. F. J., Hildebrandt, H., & Erben, T. 2010, A&A, 523, A74
Wardlow, J. L., Cooray, A., De Bernardis, F., et al. 2013, ApJ, 762, 59
Weiss, A., De Breuck, C., Marrone, D. P., et al. 2013, ApJ, 767, 88
Weiss, A., Kovács, A., Coppin, K., et al. 2009, ApJ, 707, 1201
Wesson, R., Barlow, M. J., Matsuura, M., & Ercolano, B. 2015, MNRAS, 446, 2089
Whitaker, K. E., Franx, M., Leja, J., et al. 2014, ApJ, 795, 104
Wyder, T. K., Treyer, M. A., Milliard, B., et al. 2005, ApJL, 619, L15
Zitrin, A., Labbé, I., Belli, S., et al. 2015, ApJL, 810, L12